JOURNAL OF GEOPHYSICAL RESEARCH, VOL. 86, NO. C7, PAGES 6481–6498, JULY 20, 1981

On the Detectability of Ocean Surface Waves by Real and Synthetic Aperture Radar

WERNER R. ALPERS

Universität Hamburg, Institut für Geophysik and Max-Planck-Institut für Meteorologie, Hamburg, West Germany

DUNCAN B. ROSS

National Oceanic and Atmospheric Administration, Atlantic Oceanographic and Meteorological Laboratories Sea-Air Interaction Laboratory, Miami, Florida 33149

CLIFFORD L. RUFENACH

National Oceanic and Atmospheric Administration, Environmental Research Laboratories Wave Propagation Laboratory, Boulder, Colorado 80302

Real and synthetic aperture radars have been used in recent years to image ocean surface waves. Though wavelike patterns are often discernible on radar images, it is still not fully understood how they relate to the actual wave field. The present paper reviews and extends current models on the imaging mechanism. Linear transfer functions that relate the two-dimensional wave field to the real aperture radar (SLAR) image are calculated by using the two-scale wave model. It is noted that a description of the imaging process by these transfer functions can only be adequate for low to moderate sea states. Possible other mechanisms that contribute to the visibility of waves by real aperture radar at higher sea states, such as Bragg scattering from spontaneously generated short waves at peaked crests or in wave breaking regions, and Rayleigh scattering from air bubbles entrained in the water and from water droplets thrown into the air by breaking waves, are discussed in a qualitative way. The imaging mechanism for synthetic aperture radars (SAR's) is strongly influenced by wave motions (i.e., by the orbital velocity and acceleration associated with the long waves). The phase velocity of the long waves does not enter into the imaging process. Focusing of ocean wave imagery is attributed to orbital acceleration effects. The orbital motions lead to a degradation in resolution which causes image smear as well as a SAR inherent imaging mechanism called velocity bunching. The parameter range for which velocity bunching is a linear mapping process is calculated. It is shown that linearity holds only for a relative small range of ocean wave parameters: The likelihood that the transfer function is linear increases as the direction of wave propagation approaches the range direction, as the wavelength increases, and as the wave height decreases. Linearity is required for applying simple linear system theory for calculating the ocean wave spectrum from the gray level intensity spectrum of the image. Although, in general, the full ocean wave spectrum cannot be recovered from the SAR image by applying simple linear inversion techniques, it is concluded that for many cases in which the ocean wave spectrum is relatively narrow the dominant wavelength and direction can still be retrieved from the image even when the mapping transfer function is nonlinear. Finally, we compare our theoretical models for the imaging mechanisms with existing SLAR and SAR imagery of ocean waves and conclude that our theoretical models are in agreement with experimental data. In particular, our theory predicts that swell traveling in flight (azimuthal) direction is not detectable by SLAR but is detectable by SAR.

A. INTRODUCTION

Among the various microwave techniques developed for measuring ocean surface waves from aircraft or satellites, imaging radars are considered to contain the greatest amount of information. They have the potential of measuring wavelength, wave direction, and wave height of the ocean waves. However, the radar image is not a one-to-one map of the imaged scene on the ocean surface. Some ocean waves are not imaged by the radar, thus making it impossible to recover the full two-dimensional ocean wave spectrum from radar images. Nonimaging occurs, e.g., when the radar transfer function, which describes the connection between the real wave field and the radar image, is so small that the radar signal drops below noise level for certain ocean wave parameters. In this paper we will discuss two types of imaging radars: (1) the Real Aperture Radar, also called Side-Looking Airborne Radar (SLAR), and (2) the Synthetic Aperture Radar (SAR). The mechanism by which ocean waves are imaged are different for SLAR and SAR. One consequence of this difference is that certain ocean waves, which cannot be seen on SLAR images, are visible on SAR images and vice-versa.

For a real aperture radar system the modulation of the radar cross section by the long ocean waves is responsible for the formation of wave images. At present the cross-section modulation is not well known, through first experiments with the aim of measuring the modulation transfer function in the ocean have been performed during JONSWAP-75 [*Alpers and Jones*, 1978] and during the West Coast Experiment [*Wright et al.*, 1980]. In addition, simplified theoretical models for describing this modulation have been developed by *Keller and Wright* [1975], *Alpers and Hasselmann* [1978], and *Valenzuela and Wright* [1979]. Given this incomplete knowledge of the cross-section modulation transfer function, we will discuss the consequences for SLAR imagery of ocean waves.

For synthetic aperture radar systems, in addition to cross-section modulation, the orbital motion of the water particles associated with the long ocean surface waves can play a domi-

Paper number 1C0120.
0148-0227/81/001C-0120$01.00

nant role in the image formation [see, e.g., *Larson et al.,* 1976; *Elachi and Brown,* 1977; *Alpers and Rufenach,* 1979; *Swift and Wilson,* 1979; *Valenzuela,* 1980; *Rufenach and Alpers,* 1981]. This imaging mechanism is a SAR inherent artifact. It is caused by the fact that SAR finds cross-range (azimuth) location of a target via the Doppler coordinate and that the motions of a target in the range direction belies this relation.

When ocean surface waves are imaged, then the elements (facets) of the scene have varying radial velocities which lead to a nonuniform displacement of the scatter elements in the image plane. As a consequence, the density of the scatter elements in the image plane varies in flight direction and thus produces wavelike patterns in the SAR image ('velocity bunching').

In addition to this velocity-induced SAR imaging mechanism the orbital accelerations cause a degradation in radar resolution in flight (azimuthal) direction. The degradation in azimuthal resolution varies along the flight direction and thus can also contribute to the formation of wavelike patterns in the SAR image. However, for certain ocean wave parameters the orbital motions lead to an image smear such that no wave patterns are discernible on the SAR image [*Rufenach and Alpers,* 1981].

In a recent paper, *Raney* [1980] has pointed out that the azimuthal resolution is also degraded by the finite coherence time of the scene. However, it has been shown by *Rufenach and Alpers* [1981] that the coherence time relevant for ocean wave imaging by SAR is usually of the order of a few seconds. This implies that for most radars the finite scene coherence time has only a small influence on the degradation in azimuthal resolution.

In section B we discuss the relevant imaging mechanism for detecting ocean surface waves by real aperture radars, and in section C, the imaging mechanism for synthetic aperture radars. Then, in section D we present examples of existing SLAR and SAR images of ocean waves obtained from aircrafts and the SEASAT satellite and compare them with our theoretical predictions. Finally, in section E the results obtained in this paper are summarized.

B. Imaging of Ocean Surface Waves by Real Aperture Radar

1. *Bragg Scattering in the Two-Scale Wave Model*

The detectability of ocean waves by real aperture radar becomes possible by the modulation of the radar cross section by the long ocean waves. For low to moderate sea states there exists presently only one theoretical model capable of describing this modulation which we shall call here, for brevity, the linear modulation theory [*Keller and Wright,* 1975; *Alpers and Hasselmann,* 1978]. This linear (i.e., weak modulation) theory is essentially based on the two-scale ocean wave model introduced by *Wright* [1968] for the description of microwave scattering by the rough sea surface. In this model, Bragg scattering by the ocean surface ripples is the relevant scattering mechanism for oblique incidence angles.

The cross-section modulation by the long ocean waves is attributed to two effects: (1) the tilt modulation and (2) the hydrodynamic modulation, which is assumed to be describable by a weak interaction theory (WKB-type interaction theory). The modulation is described mathematically by a modulation transfer function $R(\vec{k})$, which is defined by [see, e.g., *Alpers and Hasselmann,* 1978]

$$\sigma = \sigma_0 + \delta\sigma = \sigma_0 \left[1 + \int (R(\vec{k}) z(\vec{k}) e^{i(\vec{k}\vec{x} - \hat{\omega} t)} + \text{c.c.})\, d\vec{k} \right] \tag{1}$$

σ is the normalized radar cross section and $z(\vec{k})$ the Fourier transform of the surface elevation ζ associated with the long waves:

$$\hat{\zeta} = \int (z(\vec{k}) e^{i(\vec{k}\vec{x} - \hat{\omega} t)} + \text{c.c.})\, d\vec{k} \tag{2}$$

$\vec{k}$ and $\hat{\omega}$ are the wave vectors and radian frequencies of the large-scale wave field, and c.c. stands for complex conjugate. We assume that the cross-section modulation depends linearly on the long wave field, which implies that $R(\vec{k})$ does not depend on $z(\vec{k})$. This is a rather strong assumption, but it has proven to be a useful one, at least for modeling microwave backscattering at the sea surface for low to moderate sea states. If only one ocean wave were present, e.g., a monochromatic swell, then (1) could also be written as

$$\sigma = \sigma_0 [1 + |R|\, \hat{\zeta}_0 \cos(\vec{k}\vec{x} - \hat{\omega} t + \delta)] \tag{3}$$

where $\hat{\zeta}_0$ is the wave amplitude and

$$\delta = tg^{-1} \left(\frac{\text{Im}\, R}{\text{Re}\, R} \right) \tag{4}$$

In our model the complex modulation transfer function R is a sum of two terms, one describing the tilt modulation and the other the hydrodynamic modulation,

$$R = R^{\text{tilt}} + R^{\text{hydr}} \tag{5}$$

a. Tilt modulation. The tilt modulation is due to the purely geometric effect that Bragg scattering waves are seen by the radar at different local incidence angles depending on their location on the long waves. R^{tilt} can easily be calculated in the two-scale wave model or wave-facet model. We obtain (see appendix)

$$R^{\text{tilt}} = R_{\parallel} + R_{\perp} \tag{6}$$

with

$$R_{\parallel} = \frac{1}{\sigma_0} \frac{\partial \sigma}{\partial tg\psi} \bigg|_{\psi=0} i\hat{k}_{\parallel} = \frac{1}{\sigma_0} \frac{\partial \sigma}{\partial \psi} \bigg|_{\psi=0} i\hat{k}_{\parallel} \tag{7a}$$

$$R_{\perp} = \frac{1}{\sigma_0} \frac{\partial \sigma}{\partial tg\psi} \bigg|_{\delta=0} i\hat{k}_{\perp} = \frac{1}{\sigma_0} \frac{\partial \sigma}{\partial \delta} \bigg|_{\delta=0} i\hat{k}_{\perp} \tag{7b}$$

$tg\psi = \partial\zeta/\partial x$ is the slope of the long ocean wave in the plane of incidence of the incoming electromagnetic radiation and $tg\delta = \partial\zeta/\partial y$ the slope perpendicular to the plane of incidence. $\hat{k}_{\parallel}$ and $\hat{k}_{\perp}$ are the components of the wave vector of the long wave in and perpendicular to the look direction of the antenna, respectively. In Figure 1 the dimensionless components of the tilt modulation transfer function $-R_{\parallel}/i\hat{k}_{\parallel}$ and $-R_{\perp}/i\hat{k}_{\perp}$ are plotted as function of incidence angle θ for both horizontal/horizontal (*HH*) and vertical/vertical (*VV*) polarizations. The plots in Figure 1*a* apply for *L* band radars operating at a frequency of 1.2 GHz and Figure 1*b* for *X* band at a frequency of 10 GHz. The calculations have been carried out with dielectric constants $\varepsilon = 73 - 85i$ (*L* band) and $\varepsilon = 48 - 35i$ (*X* band).

From Figure 1*a* and Figure *b* it is evident that the tilt mod-

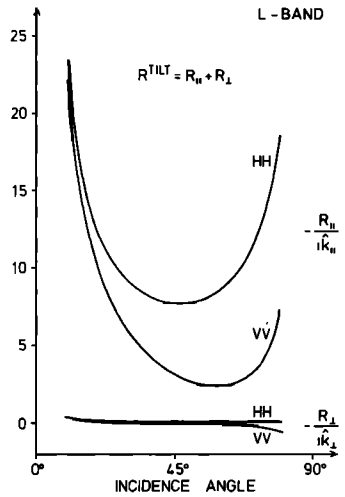

Fig. 1*a*

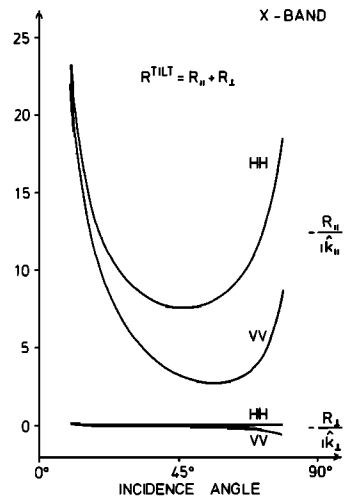

Fig. 1*b*

Fig. 1. Dimensionless tilt modulation transfer functions as a function of incidence angle for *HH* and *VV* polarizations. The upper two curves apply for scattering at range traveling waves and the lower curves for scattering at azimuthally traveling waves. (*a*) *L* band radars; (*b*) *X* band radars.

ulation is practically identical for *L* and *X* band. We also note that the tilt modulation is larger for *HH* polarization than for *VV* polarization, although the cross section itself is smaller for *HH* polarization than for *VV* polarization [see *Wright,* 1968; *Valenzuela,* 1978]. Furthermore, the plots show that the tilt modulation for waves propagating perpendicular to the plane of incidence (i.e., in cross-range direction) is roughly 1 order of magnitude smaller than for waves traveling parallel to the plane of incidence (i.e., in range direction).

Note, that the tilt modulation transfer function is a purely imaginary quantity, which means that tilt modulation and wave amplitude are out of phase by 90°. The sign is such that for an up-wave ('up-wind') looking antenna maximum tilt modulation occurs at the forward face of the wave.

b. Hydrodynamic Modulation. The hydrodynamic contribution of the cross-section modulation is characterized by a nonuniform distribution of the short waves with respect to the long ocean wave field, which is attributed to interactions between short and long waves. The simple hydrodynamic interaction theory described by *Keller and Wright* [1975] and *Alpers and Hasselmann* [1978] can only be valid for a relatively smooth sea, where nonlinear effects, which lead to a steepening of waves and eventually to wave breaking, are unimportant. Note also that nonuniform surface wind drifts that might be induced by the wave field [*Phillips and Banner,* 1974] are not included in this hydrodynamic interaction theory.

In this theory the hydrodynamic modulation transfer function in its most general form is given by [see *Alpers and Hasselmann,* 1978]

$$R^{hydr}(\hat{\mathbf{k}}, \mathbf{k}) = \frac{\hat{\omega} - i\mu}{\hat{\omega}^2 + \mu^2} \frac{\hat{\omega}}{|\hat{\mathbf{k}}|} (\mathbf{k} \cdot \hat{\mathbf{k}}) \left[\frac{1}{E_0} \hat{\mathbf{k}} \cdot \frac{\partial E_0}{\partial \mathbf{k}} - \gamma \frac{\mathbf{k} \cdot \hat{\mathbf{k}}}{|\mathbf{k}|^2} \right] \quad (8)$$

where $\mathbf{k}$ is the wave number of the Bragg scattering wave, E_0 the spectrum of the short waves in wave number space, $\gamma = 1/2$ for gravity waves, and μ ($\mathbf{k}$, $\mathbf{x}$) an unknown parameter which has to be determined by experiment; μ^{-1} has the dimension of time and is also called 'relaxation time constant.'

Suppose that the short wave spectrum E_0 is a Phillips spectrum, $E_0 \sim |\mathbf{k}|^{-4}$, then (8) takes the simple form

$$R^{hydr}(\hat{\mathbf{k}}, \mathbf{k}) = -4.5\, |\hat{\mathbf{k}}|\, \hat{\omega}\, \frac{\hat{\omega} - i\mu}{\hat{\omega}^2 + \mu^2} \cos^2(\hat{\mathbf{k}}, \mathbf{k}) \quad (9)$$

For $\mu = 0$, this theory reduces to that of *Longuet-Higgins and Stewart* [1964], which yields the maximum of the short wave energy at the crests of the long waves. However, for $\mu \neq 0$, a nonvanishing phase shift between the maximum of the short wave spectral energy and the wave crest occurs (see Figure 2). A consequence of such a phase shift is that the upwind and downwind cross sections are different, a fact that has been confirmed in many microwave backscattering experiments [see, e.g., *Daley et al.,* 1970; *Daley et al.,* 1971].

We note that the hydrodynamic transfer function is proportional to $\cos^2(\hat{\mathbf{k}}, \mathbf{k})$ or $\sin^2\Phi$, where Φ is the angle between the flight (azimuth) direction and the direction of propagation of the long ocean wave. This implies in particular, that those components of the short wave field which travel perpendicular to a long ocean wave are not modified, i.e., they neither gain nor lose energy to the long waves, and thus do not contribute to the cross-section modulation. However, it should be stressed that such a modulation is only absent in our first-order theory. Indeed, we expect that this theory is not applicable for high sea states. In this case, the short waves that travel perpendicular to the long waves are modulated due to higher-order effects, e.g., by wave-wave interaction among the short gravity waves. An extension of this theory to second order has recently been developed by *Valenzuela and Wright* [1979].

Furthermore, we expect that this simple hydrodynamic interaction theory is better applicable for the modulation of surface waves with wavelengths in the decimeter range than in the centimeter range. This is because the distribution of the shorter ripple waves is more strongly affected by the wind than the distribution of the longer ripple waves. A nonuniform generation of surface ripples by the wind, e.g., by a wave-induced spatially varying air flow, should manifest itself stronger in the centimeter than in the decimeter wave regime. But our theory does not include such a nonuniform wave generation mechanism by the wind.

The distribution of the decimeter waves is mainly determined by hydrodynamic interaction processes. They are more in an equilibrium state than the shorter centimeter waves, and

thus their distribution can be calculated from a source function that describes only a slight deviation from equilibrium. In this theory, the input from the wind, the energy transfer within the wave field due to conservative resonant wave interaction, and the energy loss due to dissipative processes are lumped into one single source term proportional to the action density associated with the short waves [*Alpers and Hasselmann,* 1978]. The hydrodynamic interaction theory described above is therefore a 'near-equilibrium' theory. Thus, we expect that this theory is better applicable to L band radar imagery of ocean waves than to X band imagery, because the wavelength of the Bragg scattering waves for L band radar backscattering is in the decimeter range, whereas for X band radar backscattering it is in the centimeter range. Measurements of the radar cross-section modulation transfer function in the ocean have shown that for low to moderate sea states the modulation is of the same order as predicted by this theory [*Alpers and Jones,* 1978; *Wright et al.* 1980].

There seems to be experimental evidence from data obtained during the JONSWAP-75 (Joint North Sea Wave Project 1975) experiment and the West Coast Experiment [*Wright et al.,* 1980] that the modulation depends on wind speed W and wind direction. In particular, the modulation decreases with increasing wind speed. Within the above theory, this would require us to abandon the concept of a constant relaxation time constant μ^{-1}. But most probably, it does not suffice just to introduce a wind speed dependent relaxation time constant $\mu^{-1}(W)$. Instead, the wind input has to be included more explicitly in the theory in order to describe adequately the measured hydrodynamic modulation. An enhanced short wave modulation by wave induced airflow can be obtained by adding a forcing term in the radation balance equation (this is the basic equation from which (8) was derived) which is porportional to the long wave slope. We only mention this idea briefly since it is beyond the scope of the present paper to develop such an improved hydrodynamic interaction theory. If further modulation experiments in the ocean should confirm this dependence on wind speed and wind direction, then it would be necessary to measure the wind simultaneously in order to extract wave height spectral information from the cross-section modulation patterns. This might be achieved by measuring the magnitude of the radar cross section and by using semiempirical relations to convert cross section information into wind information [*Jones et al.,* 1981].

2. *Backscattering Mechanisms for High Sea States*

As was pointed out in the last section, we do not expect that the linear modulation theory based on the two-scale wave model is applicable for high sea states. For example, it has been observed by several investigators [*Yeschenko and Lande,* 1972; *Long,* 1974; *Fontanel et al.,* 1979; *Lewis and Olin,* 1980; G. P. de Loor, private communication, 1979] that the radar return from the sea surface sometimes exhibits a spikey character ('sea spikes').

Long [1974] reports that this occurs when the waves break (50% of the time) or almost break (40% of the time), and that the frequency of occurence of spikes is greater at *HH* than at *VV* polarization. In the case of almost breaking waves, the wave has a very peaked crest. One possible contribution to an enhanced radar cross section would be that at these steep crests Bragg waves are spontaneously generated by strong hydrodynamic interactions. Another conceivable backscattering mechanism is Rayleigh scattering by air bubbles and spray produced in wave breaking regions.

a. Bragg scattering at waves generated by strong hydrodynamic interactions. Spontaneous generation of short waves has been observed many times in wave tank experiments [*Chang et al.* 1978; O. H. Shemdin, private communication, 1979], and one would expect that the phenomenon also occurs in the open ocean [see also *Phillips,* 1977]. According to *Yeschenko and Lande* [1972], this happens sporadically even for low amplitude swell in the absence of wind. From theoretical considerations, one expects that the shorter wavelengths are the most important in this process. This implies that the radar cross section at or near the wave crest is larger for X band than for L band radars, and this would result in a higher contrast in the X to K band (8.0–40.0 GHz) imagery than in L band (1.0–2.0 GHz) imagery. Furthermore, it has been observed that the short waves generated at the crests have a broad directional distribution. This implies that the Bragg scattering cross section associated with waves generated by strong hydrodynamic interactions is only weakly dependent on azimuth angle. If Bragg scattering at these waves is the dominant scattering mechanism for a given (high) sea state, then the detectability of ocean waves on SLAR images should be almost independent of the angle between wave and radar look direction.

Furthermore, we expect that the spectral energy density of the waves generated by strong hydrodynamic interactions is asymmetrically distributed with respect to the long wave crests, or more precisely, the energy density is larger on the leeward face of the long wave than on the luffward face. This leads to a large upwind/downwind ratio of the radar cross section, which has often been observed, especially for X band. It has been reported by *Daley et al.* [1970, 1971], that the ratio is larger for X band than for L band. *Fontanel* [1978] reports an upwind/downwind ratio of 6 dB for 8–9 m/s winds and significant wave heights of 0.7–1.6 m at X band. Linear modulation theory can only give an upwind/downwind ratio of approximately 1.5 dB.

The 'spikeyness' of radar return is therefore clearly related to amost breaking and actively breaking waves. The magnitude of the spikes has been observed to be 10–15 dB, depending upon the frequency and resolution of the particular radar [see e.g., *Fontanel et al.,* 1979]. Therefore, we expect that the sea spikes are an important phenomenon in the wave imaging for high sea states.

3. *Rayleigh Scattering*

When waves break, water droplets of varying size are thrown into the air, and air is trapped creating bubbles within the water body. Microwave energy is strongly scattered by spheres with dielectric constants much different from the surrounding medium. The scattering is called Rayleigh scattering and is significant for $(d/\lambda_0) \lesssim 0.01$, where d is the diameter of the sphere and λ_0 the radar wavelength. The cross section for Rayleigh scattering increases with the fourth power of d/λ_0

$$\sigma^{\text{Rayleigh}} \sim \left(\frac{d}{\lambda_0}\right)^4 \tag{10}$$

Note, that the occurrence of foam in itself is not associated with an increase in radar cross section. Foam can be considered to form an 'impedence match' to the water surface, and thus white water reduces the radar return. This implies that windstreaks which occur at high windspeeds and which are

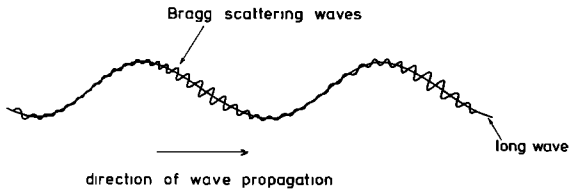

Fig. 2. Asymmetric distribution of Bragg scattering waves on the long wave due to hydrodynamic interactions.

aligned in the direction of the wind appear as dark streaks on (positive film) radar images.

Rayleigh scattering is almost independent of incidence and azimuth angle. Small angular dependences can occur because the number of scattering spheres contributing to a pixel element depends on the geometry.

If Rayleigh scattering were the dominant scattering mechanism, then the visibility of ocean wave patterns should only weakly depend on radar look angle. Also, the crest to trough contrast should be larger for K_a band ($\lambda_0 \approx 10$ mm) than for L band radars, because of the λ_0^{-4} dependence of the cross section. Furthermore, no strong dependence on polarization should occur. However, since average bubble and spray diameters are 3–4 orders of magnitude less than the wavelength of radars operating in the centimeter or decimeter wavelength band [see *Kraus,* 1972], Rayleigh scattering is not generally expected to be important in the wave imaging process.

C. Imaging of Ocean Surface Waves by Synthetic Aperture Radar

The physical process which renders long ocean waves detectable by SAR images is to a large extent cross-section modulation as described in the last section for real aperture radar systems. However, because the fine azimuthal (cross-range) resolution of SAR is achieved by recording the phase history of the backscattered signal originating from targets over a finite time T (usually of the order of 1 s), the wave motions during this time are a crucial factor in the formation of SAR ocean wave images. The motion effects can be a destructive as well as a constructive factor in the imaging process, depending on the radar and ocean wave parameters involved. By destructive we mean a 'smearing' in the image or a degradation in radar resolution, and by constructive the formation of wavelike patterns in the image.

For $\hat{\omega}T/2 \lesssim 1$ it is possible to distinguish between velocity and acceleration induced effects [see *Alpers and Rufenach,* 1979; *Swift and Wilson,* 1979]. The velocity induced imaging process is called 'velocity bunching' and gives rise to the formation of wavelike patterns in the image [see, e.g., *Tomiyasu,* 1975; *Larson et al.,* 1976; *Elachi and Brown,* 1977; *Wright,* 1978; *Alpers and Rufenach,* 1979; *Swift and Wilson* 1979; *Valenzuela,* 1980; *Rufenach and Alpers,* 1981]. The acceleration, on the other hand, causes a degradation in azimuthal resolution and can also contribute to the formation of wavelike patterns.

In many cases, the wave motions enter into the SAR imaging process in a highly nonlinear way. Then the description of the mapping of the moving random sea surface onto a SAR image by a linear transfer function is not applicable.

Let us assume that the SAR is a 'perfect' instrument which maps uniquely a two-dimensional radar cross-section distribution $\sigma(x, R)$ into an image intensity distribution $I(x, R)$. Furthermore, we assume that the scattering at the rough ocean surface can be described as the scattering at an ensemble of scattering elements (facets), which are statistically independent: The phase of the scattering amplitude has a uniform and the envelope a Rayleigh probability distribution. This assumption should be valid if the scattering is predominantly due to Bragg scattering and if the facet areas are sufficiently large (typically larger than few m^2). However, more experimental data on the statistical behavior of microwave backscattering at rough ocean surfaces would be helpful for settling this controversial issue.

The ensemble-averaged SAR image intensity distribution $\langle I(x, R)\rangle$ can then be calculated from well-known formulas of SAR theory [see, e.g., *Brown,* 1967; *Harger,* 1970; *Hasselmann,* 1980]. Let us assume that range compression has already been carried out and that range-azimuth coupling can be neglected. In case of a Gaussian antenna pattern one obtains [see *Alpers and Rufenach,* 1979; *Rufenach and Alpers,* 1981]

$$\langle I(x, R)\rangle \sim \int_{-\infty}^{+\infty} \sigma(x_0 R)\, \frac{1}{\rho_a^{(N)'}(x_0, R)} \exp\left[-\left(\frac{\pi}{\rho_a^{(N)'}(x_0, R)}\right)^2 \times \left(\left(1 - \frac{\Delta V}{V}\right) x - x_0 - \frac{R}{V}\, \hat{u}_r(x_0, R)\right)^2\right] dx_0 \qquad (11)$$

Here $\rho_a^{(N)'}$ denotes the degraded azimuthal resolution due to target acceleration and finite scene coherence time, R the distance between the radar and the target (range), V the velocity of the platform, and $\hat{u}_r$ the radial target velocity. We have included the above formula an azimuthal focus adjustment parameter ΔV, which allows for a fine tuning of the azimuthal matched filter in the SAR processor. For stationary targets, $\Delta V \neq 0$ means that the processor is mismatched in azimuth. A mismatched filter leads to a defocused image. However, $\Delta V \neq 0$ may be advantageous for ocean wave imagery. This will be discussed in section C3.

1. *Degradation in Azimuthal Resolution*

The degraded azimuthal resolution due to wave motions has been derived by *Alpers and Rufenach* [1979] for one look, full-bandwidth processing and by *Rufenach and Alpers* [1981] for multilook processing. Including a finite scene coherence time τ_s [*Raney,* 1980] the formula for the degraded N look azimuthal resolution $\rho_a^{(N)'}$ reads (we refrain here and in the following to state the R dependence of the quantities explicitly):

$$\rho_a^{(N)'}(x_0) = N\rho_a\left\{1 + \frac{1}{N^2}\left[\left(\frac{\pi T^2}{\lambda_0}\, \hat{a}_r'(x_0)\right)^2 + \left(\frac{T}{\tau_s}\right)^2\right]\right\}^{1/2} \qquad (12)$$

$$= N\rho_a\left\{1 + \frac{1}{N^2}\left[\left(\frac{\pi}{4}\, \frac{\lambda_0}{\rho_a^2}\, \frac{R^2}{V^2}\, \hat{a}_r'(x_0)\right)^2 + \left(\frac{T}{\tau_s}\right)^2\right]\right\}^{1/2}$$

where $\rho_a = (\lambda_0 R/2TV)$ is the maximum achievable (one-look, full bandwidth) azimuthal resolution for stationary targets; λ_0, the radar wavelength; T, the maximum possible coherent integration time; N, the number of looks in azimuth direction; τ_s, the scene coherence time;

$$\hat{a}_r'(x_0) = \hat{a}_r(x_0) + 2\, \frac{V}{R}\, \Delta V \qquad (13)$$

$$\hat{a}_r(x_0) = -\, \xi \hat{\omega}^2 g(\Theta, \Phi) \cos(kx_0 + \alpha) \qquad (14)$$

the facet acceleration in range direction associated with a monochromatic ocean wave; x_0, the cross-range coordinate of

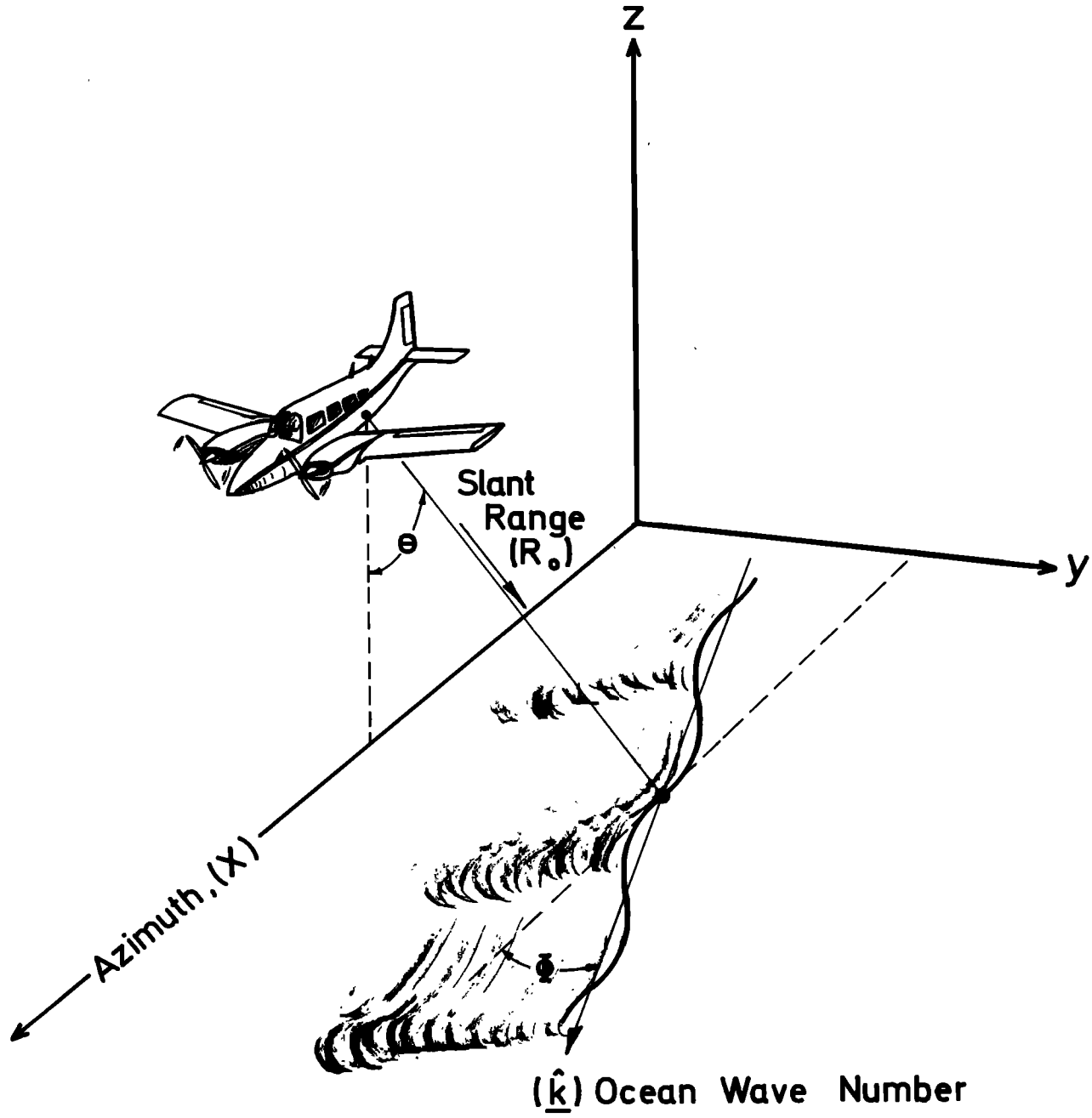

Fig. 3. Ocean wave/radar geometry; Θ is the incidence angle, Φ the azimuth angle and $\hat{k}$ the long ocean wave vector.

the facet; $\hat{\zeta}_0$, $\hat{\omega}$, $\hat{k}$ are the amplitude, radian frequency, and wave number of the long ocean wave, respectively;

$$g(\Theta, \Phi) = (\sin^2 \Theta \sin^2 \Phi + \cos^2 \Theta)^{1/2} \quad (15a)$$

$$\alpha = tg^{-1}\,(tg\,\Theta \sin \Phi) \quad (15b)$$

Θ is the incidence angle; and Φ, the azimuth angle (Φ = 0 for waves traveling in cross-range direction).

The geometry is illustrated in Figure 3. To keep this analysis conceptually simple we have refrained from approximating the phase history by a second-order polynomial in a least square sense [see *Alpers and Rufenach,* 1979] but have used, instead, the Taylor series expansion around $t = 0$. For most cases, this simplification is justified.

Equation (12) shows that the degradation in azimuthal resolution increases with waveheight $\hat{\zeta}_0$, wave frequency $\hat{\omega}$, and R/V ratio. Furthermore, it increases with radar wavelength λ_0 if ρ_a is kept fixed. On the other hand, if ρ_a is increased (i.e., the coherent integration time decreased) and all other parameters are unchanged, then the degradation in resolution due to wave motions becomes less pronounced.

From (12) it can be seen that $\rho_a^{(N)'}$ increases with range R. Since R can vary appreciably over the swath width if the SAR is flown on an aircraft (especially on a low flying one), $\rho_a^{(N)'}$ varies over the image in range direction. The range dependence of $\rho_a^{(N)'}$ is usually small for satellite applications.

The effect of degradation in azimuthal resolution for $N = 1$ and $\tau_s \to \infty$ is illustrated in Figure 4 for a typical X and L band radar flown on an aircraft such as the ERIM radar used in the Marineland Experiment [*Shuchman et al.,* 1977]. The maximum degraded azimuthal resolution $\rho'_{a,\max}$ (for $N = 1$, $\tau_s \to \infty$) is given as a function of ocean wavelength $\hat{\lambda}$, wave amplitude $\hat{\zeta}_0$ multiplied by the geometric function $g(\Theta, \Phi)$, and R/V ratio.

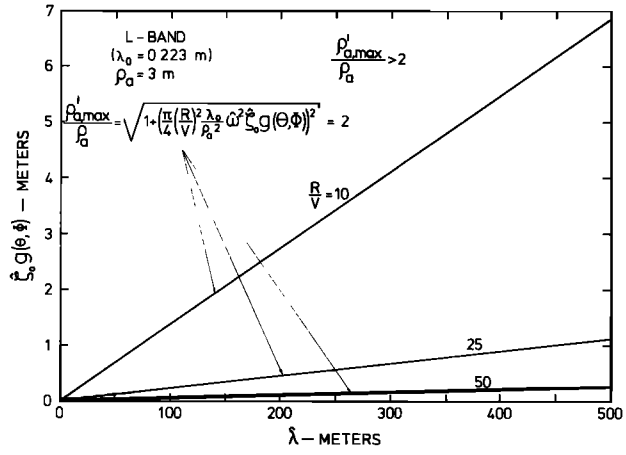

Fig. 4*a*

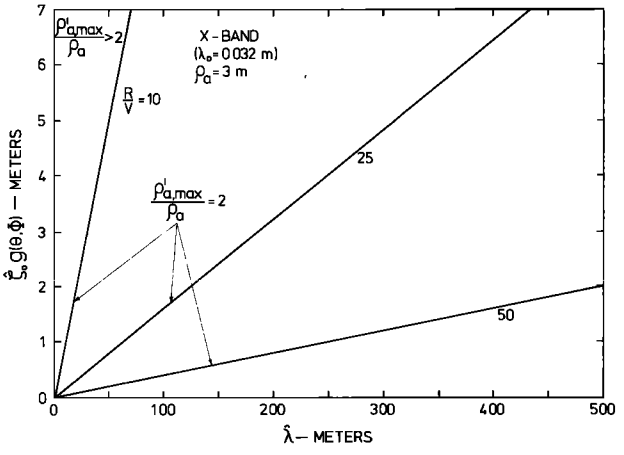

Fig. 4*b*

Fig. 4. Boundaries between parameter regions where the maximum degradation of azimuthal radar resolutions due to wave motions changes from a value smaller than 2 to a value larger than 2. The ocean wavelength is plotted on the horizontal axis, and the wave amplitude $\hat{\zeta}_0$ multiplied by the geometric factor $g(\theta, \phi)$ defined in section C1 is plotted on the vertical axis. The curves are defined by $\rho'_{a,max}/\rho_a = 2$ with R/V (in seconds) as a parameter. (*a*) Applies for an *L* band radar and (*b*) for an X band radar.

The deep water dispersion relation has been used for relating wave frequency to wavelength. The maximum degradation $\rho'_{a,max}$ was selected since the instantaneous degradation is a spatially harmonic function. In the lower right hand area under each parametric plot (the parameter is R/V), $\rho'_{a,max}/\rho_a$ is smaller than 2, while in the upper left hand area it is larger than 2. On the curves the condition $\rho'_{a,max}/\rho_a = 2$ is fulfilled. Figure 4 a applies for an *L* band radar, while Figure 4*b* applies for an *X* band radar. From these plots it can be seen that, e.g., at typical R/V ratios of 50, the degradation in azimuthal resolution due to orbital accelerations is significant at both *L* and *X* band. The degradation is strongly dependent on the R/V ratio (quadratically for small ρ_a). $\rho_a^{(NY}$ can be minimized by flying the aircraft low and fast, thereby reducing R/V.

Furthermore, (12) shows that a finite scene coherence time τ_s also degrades the azimuthal resolution. But how large is the secene coherence time when SAR is applied for ocean surface wave imaging?

The coherence time relevant for the SAR imaging process is not the usually measured correlation time τ_f for sea clutter radar return [*Trunk*, 1972; *Long*, 1975], which is of the order of 10 to 100 ms. Instead, the scene coherence time τ_s that enters into (12) and that may limit the azimuthal resolution is of the order of $1/\delta\omega$, where $\delta\omega$ is the spectral width of the backscattered signal originating from one resolution cell. If Bragg scattering is the dominant scattering mechanism, then $\delta\omega$ is the width of the Bragg line. This width depends on the size of the resolution cell relative to the large-scale structure of the ocean surface, i.e., relative to the long wave field.

The preceeding statements follow immmediately from the two-scale wave model. The backscattered signal originating from one facet exhibits fluctuations of different time scales, herein called fast and slow fluctuations. The fast random component is associated with the phase fluctuations of the short Bragg-scattering waves and is Gaussian distributed. The slower component is associated with the long wave field.

The width of the Bragg line is determined by the radial orbital velocity spread within the footprint. The associated coherence time is usually of the order of a few seconds [*Rufenach and Alpers*, 1981]. Thus, in general the orbital acceleration term in (12) should be the dominant term determining the degradation in azimuthal resolution:

$$\left|\frac{\pi T^2}{\lambda_0}\hat{a}_r'(x_0)\right| \gg \frac{T}{\tau_s} \tag{16}$$

Finally, (12) shows that the influence of orbital acceleration and scene coherence time on azimuthal resolution diminishes as the number of looks increases.

2. *Velocity Bunching*

In the case of ocean waves the velocity bunching mechanism can produce wavelike patterns on the image even if no modulation of the microwave backscattering cross section by long waves were present. In other words, given the same resolution, ocean waves which are not imaged by real aperture radars can be imaged by SAR due to this additional imaging mechanism.

Velocity bunching is caused by the fact that SAR finds azimuth location of a target via the Doppler coordinate and that the motion of a target in range belies this relation. These target motions sometimes lead to well-known peculiarities in the SAR image, e.g., that trains moving in the radial direction are

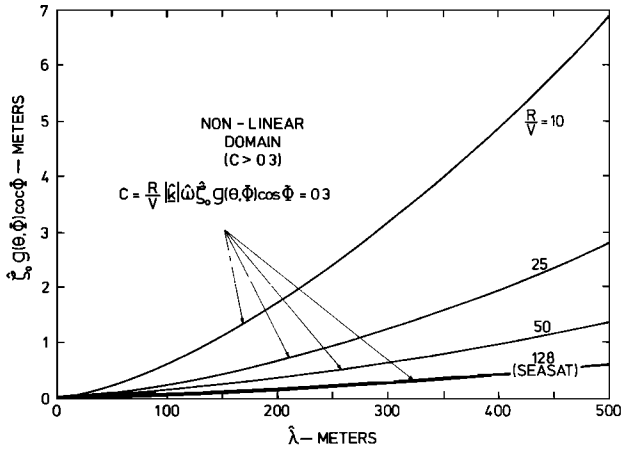

Fig. 5. Boundaries between parameter regions where the bunching modulation transfer function changes from linear to nonlinear. On the vertical axis, the ocean wave amplitude $\hat{\zeta}_0$ times $\cos\Phi \cdot g(\Theta, \Phi)$ is plotted, where Φ is the azimuthal angle. The curves are parameterized by R/V (in seconds).

not running on the railroad tracks. The shift off the tracks in azimuth direction is proportional to the train velocity projected onto the radial direction. Trains moving in opposite radial directions are shifted in opposite azimuth directions in the image.

When ocean surface waves are imaged, then the scattering elements have varying radial velocities which leads to a spatially varying, nonuniform displacement of the scattering elements in the image plane. As a consequence, the density of the scattering elements in the image plane varies in the flight direction and produces wavelike patterns in the SAR image.

For a relatively small ocean wave parameter range, velocity bunching is a linear process. This means that the ocean wave field is mapped linearly onto the radar image. Thus, velocity bunching together with tilt and hydrodynamic modulation can be described by a linear mapping transfer function. Linearity of the mapping process is desirable since in this case the ocean wave spectrum can be obtained from the radar image by first computing the spectrum of the image intensity (gray level) and then dividing it by the square of the modulation transfer function. A condition that has to be fulfilled for velocity bunching to be a linear process is [see *Alpers and Rufenach,* 1979]

$$\left|\frac{R}{V}\frac{\partial \hat{u}_r}{\partial x_0}\right| \ll 1 \tag{17}$$

where $\hat{u}_r$ is the average velocity of the facets during the SAR integration time. Furthermore, the following additional conditions have to be fulfilled in order to obtain a linear mapping process [see *Alpers and Rufenach,* 1979]: $\sigma(x_0)$ and $\rho_a^{(N)'}(x_0)$ do not vary much within the azimuthal resolution cell. $\sigma(x_0)$ is the 'real' cross-section modulation as sensed by real aperture radars.

The physical motions imparted to the scatterers on the ocean surface are due to the orbital motions associated with the long waves and thus the linearity conditions (17) can be expressed in terms of the long ocean wave parameters $\hat{\zeta}_0$, $\hat{\mathbf{k}}$, $\hat{\omega}$ and the radar parameters R, V, λ_0, Φ by

$$\left|\frac{R}{V}\frac{\partial \hat{u}_r}{\partial x_0}\right| \leq \frac{R}{V}\hat{\zeta}_0|\hat{\mathbf{k}}|\hat{\omega}\cos\Phi\, g(\Theta) \equiv C \tag{18}$$

For most radar and sea state parameters the condition (18) is the most severe one. As is evident from (28) and Figure 2 of *Alpers and Rufenach* [1979], a reasonable choice for the limit, where the mapping turns from linear to nonlinear, is given by

$$|C| \leq 0.3 \tag{19}$$

The degradation in azimuthal resolution has only very minor effects on the boundary between the linear and nonlinear domain as long as the degraded azimuthal resolution $\rho_a^{(N)'}$ is at least 4 times smaller than the ocean wavelength as has been verified by numerical calculations.

From (18), it is evident that the mapping is always linear for waves traveling in range direction ($\Phi = 90°$). Furthermore, it is also linear in an angular interval around this direction, the width of which increases when R/V or the wave amplitude $\hat{\zeta}_0$ decreases, or the wavelength $\hat{\lambda}$ increases. (Note that this linearity condition is independent of radar wavelength.)

In the linear parameter regime, velocity bunching can be described by a linear transfer function in complete analogy to tilt and hydrodynamic modulation. It is given by

$$R^{\text{bunching}} = -\frac{R}{V}\hat{k}_x\hat{\omega}\left(\frac{\mathbf{k}_x}{|\vec{k}|} - i\frac{\mathbf{k}\cdot\hat{\mathbf{k}}}{|\vec{k}|\,|\hat{\mathbf{k}}|}\right) \tag{20}$$

or, in terms of modulus and phase,

$$R^{\text{bunching}} = |R^b|\cdot e^{i\phi} \tag{21}$$

by

$$|R^b| = \frac{R}{V}|\hat{\mathbf{k}}|\,\hat{\omega}\cos\Phi\, g(\Theta,\Phi) \tag{22}$$

$$\phi = -tg^{-1}(tg\,\Theta\sin\Phi) \tag{23}$$

($\mathbf{k}$ denotes the projection of the three-dimensional radar wave vector $\vec{k}$ onto the horizontal plane).

Note that R^{bunching} vanishes for waves traveling in range direction ($\Phi = 90°$) and is maximum for waves traveling in azimuth direction ($\Phi = 0°$).

The effect of velocity bunching is illustrated in Figure 5 as a function of $\hat{\zeta}_0\, g(\Theta,\Phi)\cos\Phi$ and R/V. The maximum velocity bunching modulation C is plotted, since the instantaneous bunching is a spatially harmonic function. In the lower right-hand area under each parametric plot (parameter R/V) the condition $C < 0.3$ is fulfilled, i.e., for this parameter range, velocity bunching is a linear mapping process, while in the upper left-hand area it is a nonlinear mapping process. It can be seen from (18) and (19) that radars carried on board low and fast flying aircrafts fulfill best the linearity condition.

3. *Focus Adjustments for Moving Ocean Waves*

It has been claimed by several authors [*Jain,* 1978; *Shemdin et al.,* 1978; *Shuchman et al.,* 1978] that SAR is sensitive to the phase velocity of long ocean waves. This seems to be supported by the experimental fact that by adjusting the azimuthal focus in the SAR processor by an amount equal to the phase velocity of a long wave traveling in azimuthal direction, the image contrast (or modulation depth) is improved. In other words, the ratio of the intensities of bright and dark regions in the image of the wave field is increased when such a correction is applied to the azimuthal focus setting. In this case, the image of the ocean wave field looks sharper, it is 'in focus.'

However, the Doppler history of the SAR signal is determined by the sum of the phase velocity of the Bragg scattering wave and the orbital velocity associated with the long waves (for simplicity we neglect here ocean surface currents which also affect the Doppler history). The phase velocity of the long waves should not enter into the SAR imaging process, since SAR is a coherent linear system. (In passing we note that in contrast to SAR, the two-frequency microwave technique [*Plant,* 1977; *Alpers and Hasselmann,* 1978; *Schuler,* 1978; *Alpers et al.,* 1981] is sensitive to the phase velocity of the long waves, because it employs nonlinear signal processing).

But in order to explain the experimentally found increase in modulation depth in ocean wave imagery when the azimuthal focus setting is changed relative to stationary target imagery, it is not necessary to invoke the phase velocity of the long waves. Focusing of ocean waves can also be explained by orbital acceleration effects [*Alpers and Rufenach,* 1980].

This can be seen from (11), (12), (13), and (14). The target acceleration $\hat{a}_r(x_0)$ associated with a monochromatic wave traveling in azimuthal direction is a function of x_0. Therefore, also the azimuthal resolution $\rho_a^{(N)'}(x_0)$ is a function of x_0. By

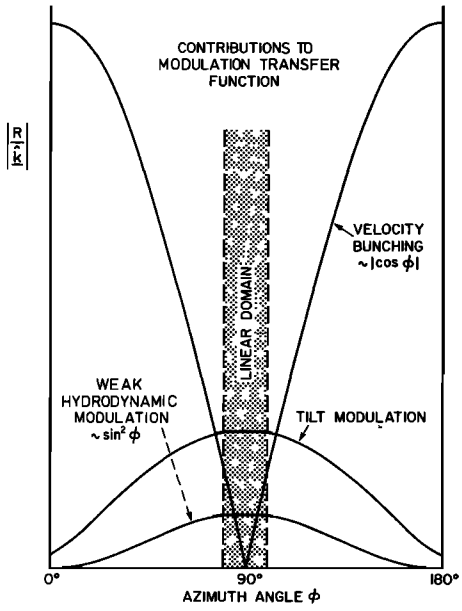

Fig. 6. The dependence of the nondimensional modulation transfer functions describing tilt, weak hydrodynamic, and velocity bunching modulation on azimuthal angle. There is a small angular interval around the range direction ($\Phi = 90°$), where velocity bunching is a linear mapping process.

varying the azimuthal focus adjustment parameter ΔV in the processor (see (13)) one can achieve $\hat{a}_r'(x_0) = 0$ at any given azimuthal location x_0 along the wave profile. At such a point the azimuthal resolution is finest, i.e., $\rho_a^{(N)'}$ attains there its smallest possible value. If $\hat{a}_r'(x_0) = 0$ coincides with the location of maximum cross section (due to tilt and hydrodynamic modulation and to velocity bunching), then the SAR image may exhibit a larger modulation depth.

The required azimuthal focus correction ΔV lies in the range

$$-\left|\frac{R}{2V}\hat{a}_r^{\max}\right| \le \Delta V \le \left|\frac{R}{2V}\hat{a}_r^{\max}\right| \tag{24}$$

where $\hat{a}_r^{\max}$ designates the maximal radial acceleration of the facet. It is given by (see (14))

$$|\hat{a}_r^{\max}| = \int_0 \hat{\omega}^2\, g(\Theta, \Phi) \tag{25}$$

It turns out that the quantity $(R/2V)\hat{a}_r^{\max}$ is often of the same order as the phase velocity of long ocean waves (typically 10 to 20 m/s). Thus, image contrast enhancement is apparently only achieved by adjusting for the phase velocity. In reality, the adjustment is made for a quantity which is associated with the orbital acceleration, and which, coincidently, happens to be of the same order of magnitude as the phase velocity of long ocean waves.

The required azimuthal focus adjustment ΔV for enhancing the modulation depth in ocean wave imagery is proportional to the ratio R/V, not to V. This implies that sensitivity to focusing is not restricted to airborne SAR's. Often the R/V ratios for airplane and satellite applications are of the same order of magnitude.

Focusing is bound to be important when the degradation in azimuthal resolution due to orbital acceleration is large.

It follows from (12) that this degradation is larger for L band than for X band (if ρ_a is kept constant) and that it increases with increasing R/V ratio.

If multi-look SAR processing in azimuth is applied, then the sensitivity of ocean wave imagery to azimuthal focus adjustments is decreased.

4. *The Mapping Transfer Function*

As has been shown in the last sections, the influence of wave motions on the formation of SAR images is small for certain radar and ocean wave parameters. In particular, a parameter region exist for which velocity bunching is a linear mapping process. Let us assume that we have a sea state such that the mapping of the wave field onto a real aperture radar image can be described by a linear transfer function $R^{\text{SLAR}} = R^{\text{tilt}} + R^{\text{hydr}}$. In this case, the synthetic aperture radar transfer function R^{SAR} is obtained by summing R^{SLAR} and the velocity bunching transfer function defined by (20):

$$R^{\text{SAR}} = R^{\text{tilt}} + R^{\text{hydr}} + R^{\text{bunching}} \tag{26}$$

If the mapping can be described by such a linear transfer function, then the ocean wave height spectrum $P_f(\mathbf{k})$ can be calculated from the gray level spectrum of the image, $P_I(\mathbf{k})$, by applying simple linear system theory. In two-dimensional wave number space, the relation reads [see e.g., *Bendat and Piersol,* 1971].

$$P_I(\mathbf{k}) = |R^{\text{SAR}}(\mathbf{k})|^2 P_f(\mathbf{k}) \tag{27}$$

On the other hand, if the mapping is nonlinear, then the superposition principle does not hold, and the result will be a distorted image of the wave field. Depending on the degree of nonlinearity, we expect that, in general, the spectrum of the radar image will be 'whiter.' This is because a sinusoidal wave is not imaged any more into a sinusoidal wave, but instead into another function, which, when Fourier analyzed, contains also higher harmonics. Thus, the high wave number portion of the image spectrum is increased or the spectrum is 'whitened.' A nonlinear transfer function tends to decrease the image constrast especially when many Fourier components of different wave numbers and wave directions are imaged. Therefore, we expect that a SAR image of a broadband ocean wave field which evolves from a nonlinear mapping process looks 'noisier' compared to an image which evolves from a linear mapping process. A highly nonlinear mapping should in this case eventually lead to a gray image. Thus, the ocean wave spectrum cannot be retrieved easily from the intensity spectrum of the SAR image.

One method for handling such a nonlinear mapping process would be to use Monte Carlo methods.

However, if the ocean wave field is almost monochromatic, i.e., if it can be described by a very narrow band spectrum, then even in case of a nonlinear transfer function the dominant wavelength and wave direction still can be retrieved from the image in most cases. Of course, there exists a lower bound on the wavelength that can be identified on the radar image. This lower bound is determined mainly by the degraded azimuthal resolution $\rho_a^{(N)'}$. In order to identify a wave train, at least two resolution cells per wavelength interval, but more realistically, three to four resolution cells per wavelength interval are required.

The mapping transfer functions are explicitly given in the previous paragraphs. In Figure 6 we display their dependence on azimuthal angle Φ. It shows that imaging due to velocity bunching disappears for waves traveling in range direction. At the same time, the mapping due to tilt and hydrodynamic modulation is maximum in range direction, whereas it almost

vanishes in azimuth direction. Therefore, waves propagating in range direction should be imaged best by SAR. Apart from the fact that the radial contrast patterns are smeared in the azimuthal direction due to the degradation in azimuthal resolution caused by orbital accelerations, the imaging mechanism for range traveling waves is the same for real and synthetic aperture radars. In all other directions, wave motion effects are bound to be important for SAR ocean wave imagery.

From Figure 6 it follows that velocity bunching is maximum for waves traveling in azimuth direction, though for most ocean wave parameters the velocity bunching transfer function is highly non-linear for this direction. A consequence is that azimuthally traveling waves that are not, or only faintly, imaged by SLAR can become detectable by SAR due to this motion induced imaging mechanism. Again, we expect that an almost monochromatic wave field with a long wavelength (in particular swell) becomes 'visible' on SAR images by this mechanism.

Another consequence we can draw from the expression for the transfer functions is the $|\hat{\mathbf{k}}|$ dependence of the gray level spectrum $P_I(\hat{\mathbf{k}})$ relative to the ocean wave spectrum $P_S(\hat{\mathbf{k}})$. For a fixed azimuthal angle we have

$$R^{\text{tilt}} \sim |\hat{\mathbf{k}}| \tag{28a}$$

$$R^{\text{hydr}} \sim \begin{cases} |\hat{\mathbf{k}}| & \text{for} \quad \mu = 0 \\ -\dfrac{i}{\mu}\,\hat{\omega}\,|\hat{k}| & \text{for} \quad \mu \gg \hat{\omega} \end{cases} \tag{28b}$$

$$R^{\text{bunching}} \sim |\hat{\mathbf{k}}|\,\hat{\omega} \tag{28c}$$

and therefore the functional dependence of $|R^{\text{SAR}}|^2$ on $|\hat{\mathbf{k}}|$ varies between $|\hat{\mathbf{k}}|^2$ and $|\hat{\mathbf{k}}|^3$ (for the deep ocean waves) depending on the relative magnitude of the transfer functions R^{tilt}, R^{hydr}, and R^{bunching}. Inserting these values into (27) yields $P_I(\hat{\mathbf{k}})$ proportional to a function which lies between $|\hat{\mathbf{k}}|^2\,P_S(\hat{\mathbf{k}})$ (slope spectrum) and $|\hat{\mathbf{k}}|^3\,P_S(\hat{\mathbf{k}})$.

In particular, for waves traveling in the range direction and imaged at *HH* polarization, the gray level spectrum should vary as $|\hat{\mathbf{k}}|^2\,P_S(\hat{\mathbf{k}})$, since in this case the tilt modulation is dominant for low to moderate sea states. Note that these relations only hold for the parameter region in which the transfer function is linear, a nonlinear mapping leads to a whiter image spectrum.

For high sea states, appropriate modulation transfer functions describing Bragg scattering at spontaneously generated waves and Rayleigh scattering at air bubbles and spray have to be included. At present, no theory exists which yields an analytical expression for these transfer functions. However, we expect that the cross-section modulation increases with wave slope and that it exhibits only a very weak dependence on azimuth angle.

At this point we would like to mention that recent measurements of the cross-section modulation transfer function $R^{\text{tilt}} + R^{\text{hydr}}$ by scatterometers mounted on sea-based platforms in the North Sea seem to show that their dependence on wave number $\hat{\mathbf{k}}$ is approximately given by

$$|R^{\text{tilt}} + R^{\text{hydr}}| \sim |\hat{\mathbf{k}}|^{1/2} \tag{29}$$

which is in contrast to (28). Such a wave number dependence would imply that for range traveling waves the SAR image spectrum behaves approximately as $|\hat{\mathbf{k}}|\,P_S(\hat{\mathbf{k}})$.

5. *Formation of Artificial Waves by Doppler Splitting*

In case of Bragg scattering the radar backscattering is caused by surface waves traveling toward and away from the antenna. These two Bragg scattering waves have opposite phase velocities, $\pm\, v_{\text{Bragg}}{}^{\text{ph}}$, which implies that the backscattered signal originating from one resolution element contains two Doppler components. Since SAR finds azimuthal location via the Doppler history, each scatter element on the sea surface is imaged into two image elements which are separated in azimuth by

$$|\Delta x| = 2\left|\frac{R}{V}\cdot v_{\text{Bragg}}{}^{\text{ph}}\cdot \sin\Theta\right| \tag{30}$$

If both Bragg components have comparable energy and $|\Delta x|$ exceeds the azimuthal resolution $\rho_a{}^{(N)'}$, then the SAR image contains double images of ocean waves. Such situation occurs when the radar beam points into the cross-wind direction. This leads to artificial spectral components in the SAR spectrum of wavelengths

$$\hat{\lambda}_{\pm} = \hat{\lambda} \pm |\Delta x| \qquad \text{and} \qquad \hat{\lambda}_{\Delta} = |\Delta x| \tag{31}$$

For SEASAT parameters ($R/V = 128$ s, $v_{\text{Bragg}}{}^{\text{ph}} = 0.61$ m/s, $\Theta = 20°$) one obtains for the separation of the double image points $|\Delta x| = 53$ m.

However, we expect that the formation of artificial waves by Doppler splitting is not an important phenomenon to be detectable in SAR images. The Doppler splitting only occurs in the azimuthal direction and only when both Doppler components have comparable amplitudes. In general, it leads to a broadening of the SAR image spectrum.

6. *Image Suppression Owing to Bandwidth Limitation*

If the velocity of the scattering elements projected onto the range direction is sufficiently high, then it can occur that the azimuthal displacement δx is so large that these targets are shifted completely out of the image. They appear as black spots in the (positive film) SAR image. This image suppression is again a SAR inherent artifact not present in SLAR imagery of moving targets.

The condition for nonimaging of a moving target with radial velocity $\hat{u}_r$ is given by

$$\delta x \equiv x - x_0 = \frac{R}{V}\,\hat{u}_r > R\beta \tag{32}$$

where $R\beta$ is the azimuthal spatial width of the real antenna pattern. It can also be expressed in terms of the along track antenna length D and the radar wavelength λ_0:

$$R\beta = R\,\frac{\lambda_0}{D} \tag{33}$$

or in terms of the 'single look' azimuthal resolution ρ_a and λ_0:

$$R\beta = R\,\frac{\lambda_0}{2\rho_a} \tag{34}$$

[see *Raney and Lowry*, 1978].

The condition that a target is 'blacked out' due to excess target motions can be expressed as

$$|\hat{u}_r| > \frac{1}{2}\lambda_0\,\frac{|V|}{\rho_a} \tag{35}$$

TABLE 1. Real Aperture Radar System Parameters

	AN/ APS-94D	APD-7/ APQ-97*	Torous
Frequency	9.315 GHz	34.85 GHz	15.0 GHz
Wavelength	3 cm	0.86 cm	2 cm
Pulse length	0.2 μs	variable	unknown
Pulse rate	750 PPS	1000 PPS	700–1000 PPS (estimate)
Antenna length	2.7 m	5.0 m	5 m
Beamwidth	0.9°	0.1°	0.1°
Nominal resolution	30 m	10 m	20 m (estimate)
Stablization	none	roll 4.0° pitch 1.5° yaw 1.5°	unknown
Polarization	*HH* or *VV*	*HH*	*HH*
Operating altitude over water	to 3,000 m	to 3,000 m	to 3,000 m
Typical incidence angle range	0–90°	0–90°/10–80°	unknown
Manufacturer	Motorola	Westinghouse	USSR

*Military version.

In radar systems theory, $|V|\ \rho_a^{-1}$ is called azimuthal Doppler bandwidth [*Harger,* 1970]. Note that for constant azimuthal bandwidth the radial velocity necessary to cause image suppression is smaller for radar operating at shorter wavelengths (e.g., *X* band radars) than for radar operating at longer wavelengths (e.g., *L* band radars). Furthermore, it follows from inequality (35) that nonimaging is more a problem for radars carried by aircrafts than by satellites, since aircraft velocities are 2 orders of magnitude smaller than satellite velocities. For example, if the ERIM *X* band system is flown at a speed of 75 m/s or 150 m/s and if the data are processed to the maximum resolution of 3 m, then 'black outs' occur when the radial target velocities are larger than 0.4 m/s or 0.8 m/s, respectively.

7. *Degradation in Range Resolution*

In the range coordinate, the influence of moving targets is much smaller than the azimuth coordinate and is often neglected. However, for ocean waves with a component traveling in the range direction, the orbital velocity influences the range location of the imaged targets especially for high resolution SAR's i.e., radars with long integrations times.

In the absence of target motion there is an inherent range change during the integration time usually called 'range curvature' [*Raney,* 1971]. If the targets are stationary or moving with a uniform velocity, then one can correct for range curvature in the processor. However, in case of an ocean wave field, nonuniform radial velocities are encountered.

Suppose that a facet is moving in the range direction with an orbital velocity $\hat{u}_r(t, x_0)$. The range change during the time interval T required to form the image is given by

$$\Delta R = \int_{-T/2}^{+T/2} \hat{u}_r(t, x_0)\, dt$$

$$= \zeta_0\hat{\omega} \int_{-T/2}^{+T/2} [-\sin\Theta \sin\Phi \sin(\mathbf{k}\mathbf{x}_0 - \hat{\omega}t + \delta)$$

$$+ \cos\Theta \cos(\mathbf{k}\mathbf{x}_0 - \hat{\omega}t + \delta)]\, dt$$

The range resolution for stationary targets is $\rho_r = c/2B_r$, where c is the speed of light and B_r is the chirp bandwidth. Suppose that $\rho_r < \Delta R$, then the radial target is always located in more than one range resolution cell during the integration time. This change in range location causes a smearing in the SAR image which is not present in real aperture radar imagery. The degraded range resolution is defined by

$$\rho_r' = \rho_r + \Delta R(x_0) \tag{37}$$

Taking the maximum value of $\Delta R(x_0)$, we obtain for small $\hat{\omega}T/2$ the inequality

$$\rho_r' \le \rho_r + \zeta_0\hat{\omega}Tg(\Theta, \Phi) \tag{38}$$

In most cases, $\zeta_0\hat{\omega}Tg(\Theta, \Phi)$ is of the order of 1 m or smaller. Applied to SEASAT SAR with $T = 2.5$ s and $\rho_r = 25$ m, (38) shows that the degradation in range resolution due to wave motions is of the order of a few percent and therefore negligible.

D. Comparisons With Experimental Data

In this section we compare theoretical predictions to real and synthetic aperture radar imagery of ocean surface waves that were available to us. The data originate from the K_a band SLAR of the National Oceanographic and Atmospheric Administration (NOAA) over various ocean regions, the Motorola *X* band SLAR, the USSR K_u band SLAR [see *Ross,* 1978; *Bondarenko et al.,* 1972; *Belousov et al.,* 1975], the *X* and *L* band SAR of the Environmental Research Institute of Michigan (ERIM) flown in the Marineland experiment [*Shuchman et al.,* 1977; *Shemdin et al.,* 1978], the Jet Propulsion Laboratory (JPL) *L* band SAR, and the *L* band SAR flown onboard

TABLE 2. Synthetic Aperture Radar System Parameters

	ERIM		JPL,	
	L Band	*X* Band	*L* Band	SEASAT
Frequency	1.3 GHz	9.3 GHz	1.22 GHz	1.28 GHz
Wavelength	0.235 m	0.032 m	0.246 m	0.235 m
Pulse length	2 μs	3 μs	2.2 μs	32 μs
Bandwidth	60 MHz	80 MHz	10 MHz	19 MHz
Operating altitude over water	10,000 m	10,000 m	10,000 m	800 km
Nominal velocity	75–150 m/s	75–150 m/s	240 m/s	6.6 km/s
Resolution	3 × 3 m	3 × 3 m	50 m	25 m × 25 m (4-look)
Integration time	1.0 s	0.15 s	2.5 s	2.5 s max (one-look)
Polarization	*HH, HV VV, VH*	*HH, HV VV, VH*	*HH VV*	*HH*

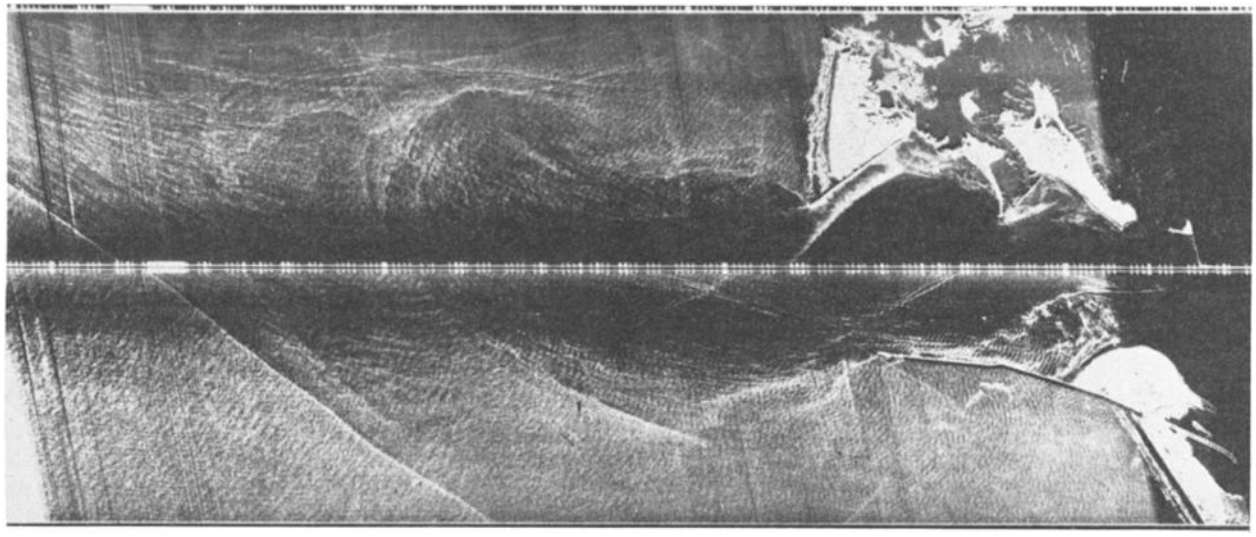

Fig. 7. K_a band SLAR imagery of the Columbia River outfall during maximum ebb tide.

the SEASAT satellite. The details of the radars are contained in Tables 1 and 2.

1. *Azimuthal Dependence*

All SLAR imagery of ocean surface waves known to the authors show that swell is not, or is very poorly imaged, when traveling in azimuthal direction. However, SLAR imagery of wind generated waves during high sea states shows very little azimuthal dependence. But still, the waves are imaged slightly better when they propagate in radial direction toward the antenna [see *Belousov et al.*, 1975]. These experimental findings are in agreement with theory, which predicts that for low sea states the SLAR imaging mechanism is strongly dependent on azimuthal angle. In particular, the (linear) modulation transfer function is 1 order of magnitude smaller for azimuthally traveling waves than for range traveling waves. However, for high sea states, the azimuthal dependence is reduced due to strong nonlinear hydrodynamic effects, leading to an almost isotropic distribution of the Bragg scattering waves.

In contrast to SLAR, synthetic aperture radar is capable of imaging azimuthally traveling swell. This has been demonstrated by airborne SAR's [see *Ross et al.*, 1974; *Teleki et al.*, 1978], as well as by the SEASAT-SAR. Good examples of azimuthally traveling swell imaged by SEASAT-SAR exist from revolution 308 on July 18, 1978, in the Pacific Ocean (32°N, 118°W) and from revolution 1044 on September 8, 1978, in the North Atlantic (area between Scotland and Iceland).

2. *Shoaling Waves*

When a wave propagates into shallow water, its length is shortened and its height increased until, finally, the wave breaks. Figure 7 is an example of K_a band SLAR imagery of the mouth of the Columbia River, on the Pacific Coast of the United States. Surface winds present at the time were from about 110°N at 5–7 m/s. This image dramatically shows the entire process of wave refraction, reflection, shoaling, and breaking. A swell of about 1 m in height was observed to be traveling toward about 110° in deep water. The swell was poorly imaged in range and not at all in azimuth direction when in deep water. Upon entering the region just to the north and west of the north jettie (see Figure 8), the waves are strongly refracted by the bottom topography. As the waves shoal, they become much more pronounced in the image until they break on the beach. The breaking region is of particular interest, since the crests of the waves are regions of greatly enhanced backscattering. Many dark areas occur in the troughs and just seaward of the surf zone. At K_a band, the wavelength of the radar, 8 mm, is 2 orders of magnitude larger than the diameter of the majority of the bubbles forming a whitecap [*Kraus*, 1972] created in the breaking process. Thus, provided that the number of bubbles is sufficinetly large, Rayleigh scattering could be an important scattering mechanism, since the condition $(\alpha/\lambda_0) < 0.01$ is fulfilled. Just south of the north jetty, however, is a region of strong backscatter comparable to that in the surf zone. The imagery was obtained during maximum ebb tide and therefore we conclude that this is a region of strong current gradient where the shortest waves are strongly refracted and strained. Color photography of the area shows that no whitecaps or foam are present. Rather, the area appears optically darker than the adjacent regions, a typical effect of increased roughness. The radar backscattering is, therefore, undoubtably due to Bragg waves, which are strongly modulated. Since the wave breaking process is also associated with strong current gradients, as well as plunging water [see *Ling et al.*, 1978], it appears that Bragg rather than Rayleigh scattering is responsible for the greatly enhanced backscatter characteristic of breaking waves as predicted in section B3.

Figures 9 and 10 show examples of X and L band imagery of surf zones obtained by the ERIM radar during the Marineland experiment on December 15, 1975 [*Shuchman et al.*, 1977; *Shemdin et al.*, 1978].

The imagery is processed to a resolution of 5 m in azimuth and 3 m in range for the L band data, and 3 m × 3 m for the X band data. From these images it can be seen that the waves in deep water are better imaged at X band than at L band due to the smaller degradation in azimuth resolution caused by wave motions.

Breaking waves in the surf zone are associated with regions of large backscattering at both frequencies. The radial accelerations as well as the spread in radial velocities are much higher in these regions than in deep water, which leads to a stretching or smearing of targets in the azimuth direction. The

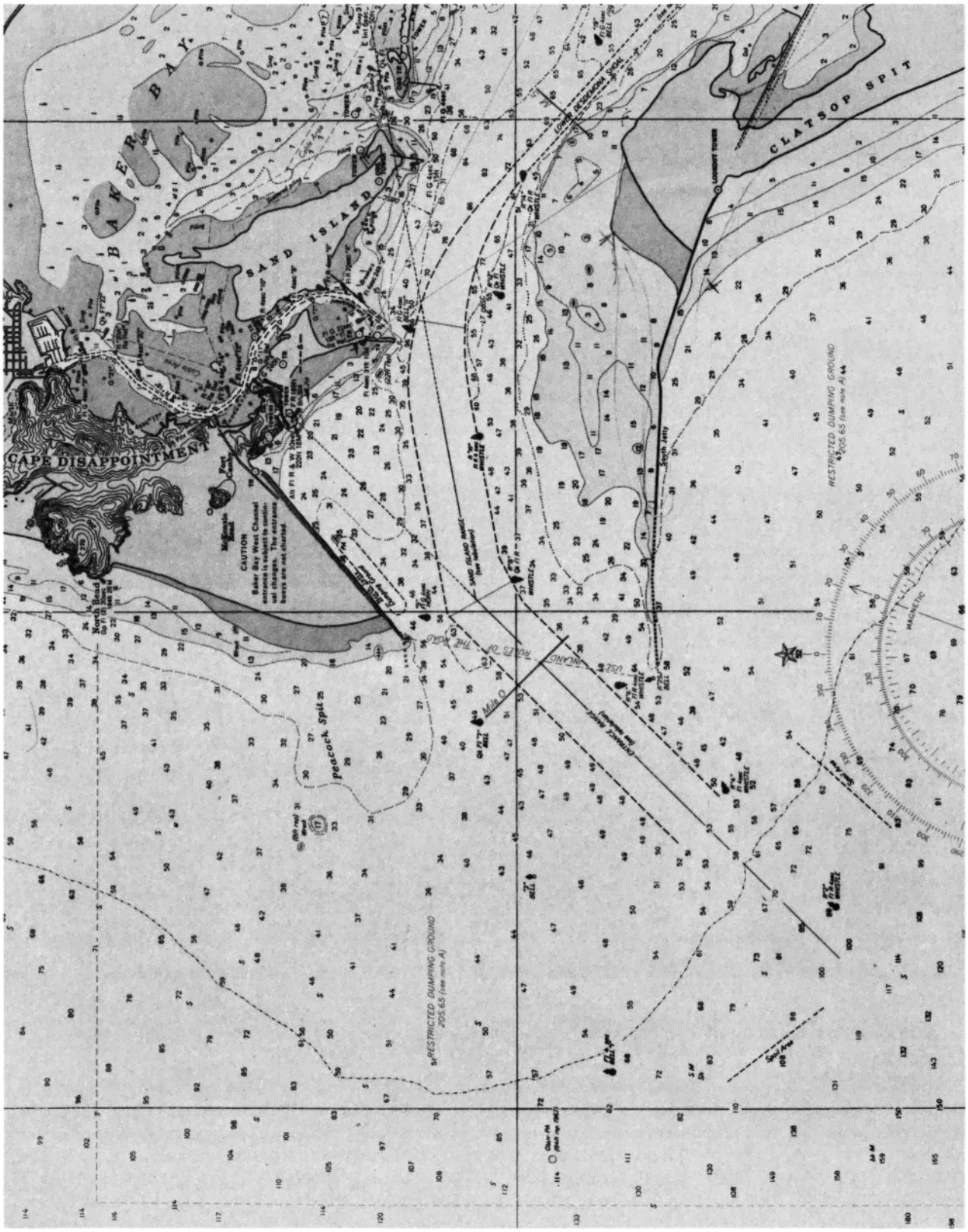

Fig. 8. Bathymetry and geography of the Columbia River outfall.

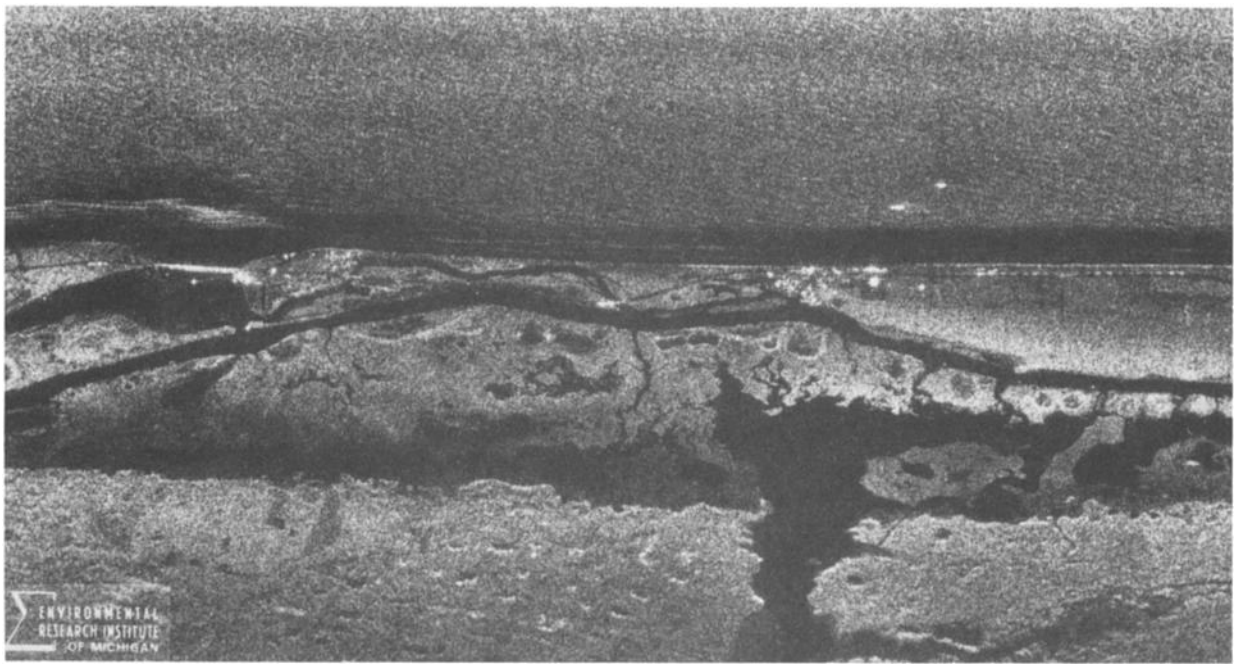

Fig. 9*a*

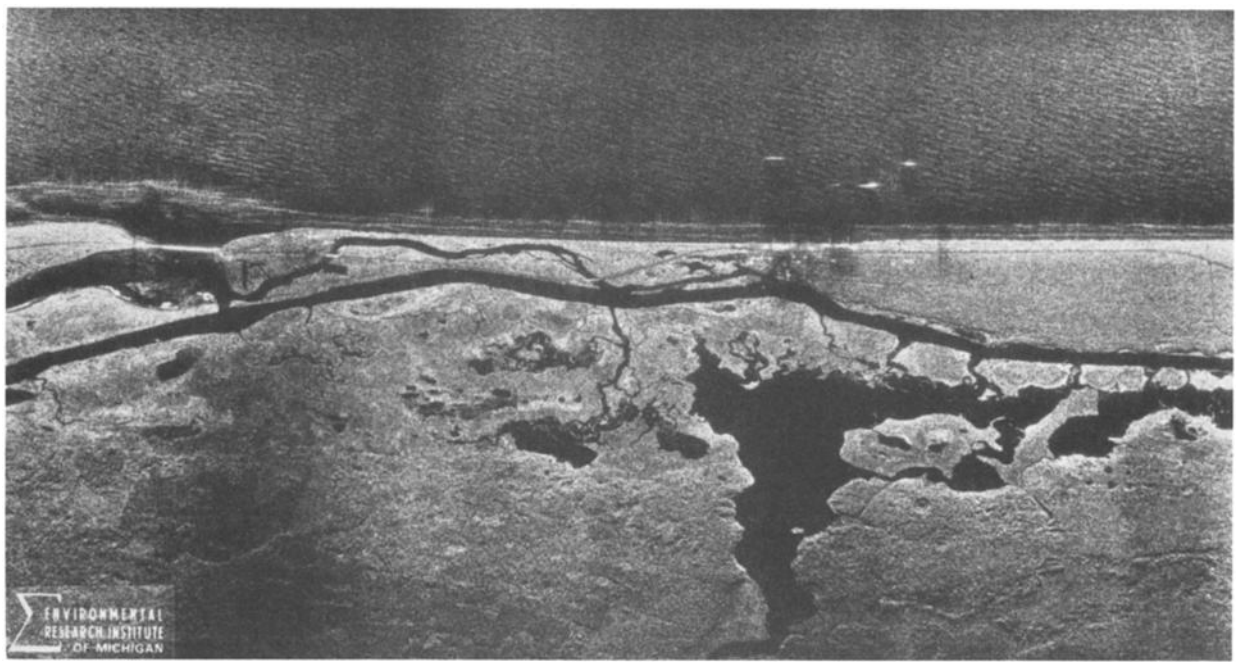

Fig. 9*b*

Fig. 9. (*a*) ERIM *L* band and (*b*) *X* band imagery of surf zone waves during the Marineland experiment (*HH* polarization) on December 15, 1975. Flight direction is parallel to the coastline.

azimuthal smearing due to velocity effects is given by $\delta x = (R/V)u_r$ (see equation (32)) which is independent of the radar wavelength. The azimuthal smearing due to acceleration effects is given by (12) and depends on the radar wavelength. From Figure 10 it can be seen that the azimuthal smearing is larger for the *L* band radar than for the *X* band radar, in accordance with (12). This smearing is also present in Figures 9*a* and 9*b*, but the stretching occurs along the wave crests.

Another feature that can occur in SAR imagery of shoaling waves is signal suppression due to limited azimuthal bandwidth as described in section C5. In the breaking part of a shoaling wave, the orbital velocity increases to the order of the phase velocity. The black regions seen in the surf zone seem to be associated partly with high velocity regions (breaking parts of the shoaling wave), exceeding the azimuthal SAR bandwidth used in this experiment. They are shifted out of the image and are therefore 'blacked out.' An additional factor in this surf zone imagery seems to be low signal suppression due to the close proximity of bright targets, especially in the *X* band radar imagery (R. A. Shuchman, private communication, 1979).

From the SLAR and SAR imagery of shaoling waves pre-

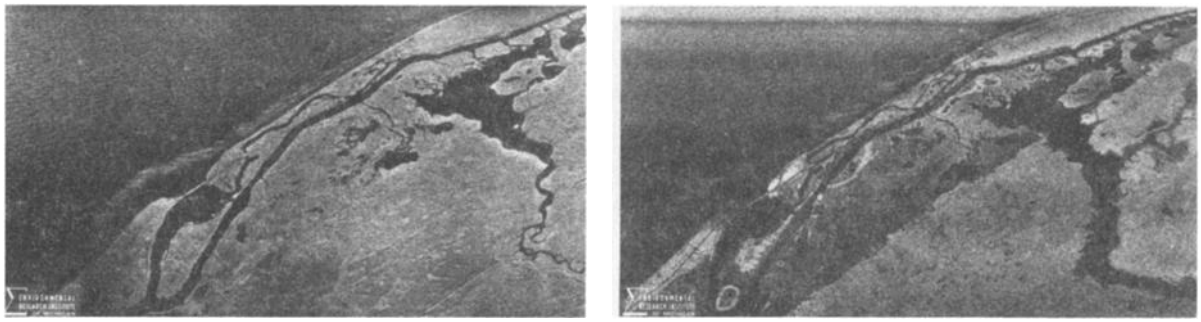

Fig. 10. Same as Figure 9 but flight direction at 45° to the coastline.

sented here, one can draw the conclusion that it is not necessary to invoke Rayleigh scattering to explain the strong radar backscattering from breaking waves, since they are almost equally well imaged by X band and L band radars. Furthermore, the K_a band data show, from the current interaction phenomenon, that even for this wavelength band a Rayleigh mechanism is not required to account for the enhanced scattering from whitecap regions.

3. *Wind Streaks*

At high wind speeds, foam is aligned in the direction of the wind, forming so-called wind streaks. According to the discussion in section B3, these streaks should be associated with low radar return. Figure 11 shows a radar image from the North Sea obtained with the NOAA K_a band SLAR during the MARSEN (Marine Remote Sensing) experiment. 'Dark' windstreaks aligned approximately in range direction and perpendicular to the wave crests are visible.

E. RESULTS

Though, at present, we have only a fragmentary knowledge of the modulation transfer function describing the variation of the radar backscattering cross section by long ocean surface waves, we have investigated, theoretically, when ocean surface waves are detectable by real and synthetic aperture radars. In addition to the 'real' cross-section modulation responsible for the imaging of ocean waves by real aperture radars, 'artificial' cross-section modulation (velocity bunching) and degradation in resolution due to wave motions are an important factor in the imaging process by synthetic aperture radars. By achieving a fine azimuthal resolution by recording of the phase history of a target over a finite time (usually of the order of 1 s), the advantage of SAR is in many cases destroyed by the very fact that the ocean wave field is moving. The relevant motion parameters are the orbital velocity and acceleration associated with the motion of the water particles.

Theoretical models for describing the imaging mechanism of ocean waves by real aperture radars exist for low to moderate sea states and have been discussed in section B. The imaging process is attributed to tilt and hydrodynamic modulation of the Bragg scattering cross section by the long ocean waves. It is pointed out that the hydrodynamic part of this modulation theory is not yet adequate. Some kind of wind dependence has to be included.

For high sea states, a proper description of the generation of short waves by breaking or nearly breaking waves has to be added. Furthermore, Rayleigh scattering from water droplets thrown into the air from air bubbles entrained in the water by breaking waves may be important for short radar wavelengths (e.g., K_a band).

From theoretical conditions, we predict for SLAR imagery of ocean waves (1) ocean waves are imaged best when traveling in the range direction (i.e., perpendicular to the flight direction); (2) swell traveling in the azimuth direction (i.e., in the flight direction) is not, or only poorly, imaged; (3) for high sea states, ocean waves are imaged at all directions, although the greatest image contrast still occurs when they travel in range direction; (4) waves are better imaged at HH polarization than at VV polarization because of the higher contribution from tilt modulation.

The prediction for SAR ocean wave imagery are (1) ocean waves traveling in range direction are best imaged. In this direction, the motion effects are the least important. The wave spectrum in range direction can be obtained from the image spectrum provided the 'real' cross-section modulation transfer function is known. (2) Swell of large wavelength is imaged when traveling in azimuth direction due to the motion induced imaging mechanism. (3) Ocean waves having large azimuthal components are, in general, smeared due to degradation in azimuthal resolution and are distorted due to the nonlinearity of the velocity bunching transfer function. As a consequence, for most ocean wave parameters, the ocean wave spectrum cannot be retrieved from the image spectrum by applying linear system theory. A broad-band wave spectrum tends to lead to a 'whiter' or broader image spectrum when the mapping transfer function is nonlinear. (4) In the special case of an almost monochromatic ocean wave field (swell) with sufficiently long wavelength, the dominant wavelength and wave direction can still be extracted from the image even when the mapping transfer function is nonlinear. (5) Breaking regions of shoaling waves are associated with large orbital velocity spreads and accelerations, which lead to azimuthal image smear. (6) The large orbital velocities encountered in the breaking regions of shoaling waves (of the order of the phase velocity) can cause 'blackouts' of these regions in the radar image due to azimuthal bandwidth limitations.

Windstreaks occurring on the ocean surface during high wind conditions appear on SLAR and SAR images as dark lines corresponding to low radar return. Rayleigh scattering at air bubbles and water droplets does not contribute significantly to the SLAR and SAR imaging mechanism at X and L band.

APPENDIX

Tilt Modulation Transfer Function

In the two-scale model, the long ocean waves are represented locally by tangent surface elements or facets on which the short waves propagate. It is assumed that Bragg scattering

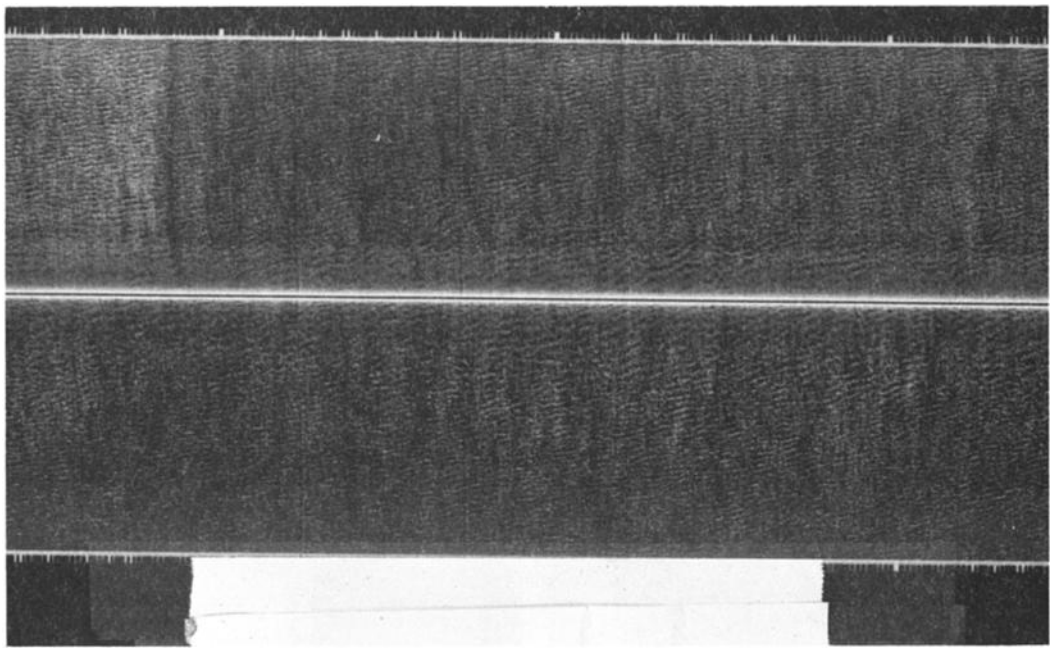

Fig. 11. Radar image of a wind sea obtained with the NOAA K_α band SLAR in the North Sea (55, 65°N, 4,81°E) on December 14, 1979, at 2323:00 h GMT from an altitude of 465 m. The heading of the aircraft is 310° N and the surface wind speed is 20 m/s from 214°N. Surface waves and dark windstreaks aligned in the direction of the wind are visible.

theory can be applied in the local reference system of the moving inclined facets.

The cross-section modulation due to tilting of the facets is then given to first order by

$$\left(\frac{\delta\sigma}{\sigma_0}\right)_{\text{tilt}} = \frac{1}{\sigma_0}\frac{\partial\sigma}{\partial\mathbf{n}}\bigg|_{\mathbf{n}=(0,0,1)}\mathbf{n} \tag{A1}$$

where $\vec{n} = (n_x, n_y, n_z)$ is the facet normal pointing into the air. In terms of the surface elevation $\xi(x, y)$ associated with the large scale wave field, we have

$$\mathbf{n} = \left[1 + \left(\frac{\partial\xi}{\partial x}\right)^2 + \left(\frac{\partial\xi}{\partial y}\right)^2\right]^{-1}\left(-\frac{\partial\xi}{\partial x}, -\frac{\partial\xi}{\partial y}, 1\right) \tag{A2}$$

Since the slopes of long ocean waves are small, it is appropriate to use the approximation

$$\begin{aligned} n_x &= -\frac{\partial\xi}{\partial x} + 0(\varepsilon^3) \\ n_y &= -\frac{\partial\xi}{\partial y} + 0(\varepsilon^3) \\ n_z &= 1 + 0(\varepsilon^2) \end{aligned} \tag{A3}$$

where

$$\varepsilon \sim \left|\frac{\partial\xi}{\partial x}\right| \sim \left|\frac{\partial\xi}{\partial y}\right|$$

Now let us assume that the wave vector $\mathbf{k}_i$ of the incident wave is in the (x, z) plane:

$$\mathbf{k}_i = k(\sin\Theta, 0, -\cos\Theta) \tag{A4}$$

where Θ is the incidence angle for a horizontal facet and $k \equiv |\mathbf{k}_i| = 2\pi/\lambda_0$.

If the facet normal deviates from the vertical by an angle ψ in the plane of incidence and by an angle δ in a plane perpendicular to the plane of incidence, then the coordinates of the facet normal are given by

$$\mathbf{n} = (\sin\psi\cos\delta, \sin\delta, \cos\psi\cos\delta) \tag{A5}$$

From the scalar product of (A4) with (A5), we obtain the local incidence angle $\tilde{\Theta}$:

$$\begin{aligned} \cos\tilde{\Theta} &= -k^{-1}(\mathbf{k}_i \cdot \mathbf{n}) \\ &= -\sin\Theta\sin\psi\cos\delta + \cos\psi\cos\delta\cos\Theta \\ &= \cos\delta\cos(\Theta + \psi) \end{aligned} \tag{A6}$$

The Bragg scattering cross section per unit area for a slightly tilted facet has been calculated by Valenzuela [see *Valenzuela,* 1968; *Valenzuela et al.,* 1971; *Valenzuela,* 1978]. For horizontal/horizontal and vertical/vertical polarizations, one obtains

$$\sigma_{0HH} = 4\pi k^4\cos^4\tilde{\Theta}\left|\left(\frac{\sin(\Theta+\psi)\cos\delta}{\sin\tilde{\Theta}}\right)^2 g_{\perp\perp}(\tilde{\Theta}) + \left(\frac{\sin\delta}{\sin\tilde{\Theta}}\right)^2 g_{\parallel\parallel}(\tilde{\Theta})\right|^2 \times E_0(2k\sin(\Theta+\psi), 2k\cos(\Theta+\psi)\sin\delta) \tag{A7}$$

$$\sigma_{0VV} = 4\pi k^4\cos^4\tilde{\Theta}\left|\left(\frac{\sin(\Theta+\psi)\cos\delta}{\sin\tilde{\Theta}}\right)^2 g_{\parallel\parallel}(\tilde{\Theta}) + \left(\frac{\sin\delta}{\sin\tilde{\Theta}}\right)^2 g_{\perp\perp}(\tilde{\Theta})\right|^2 \times E_0(2k\sin(\Theta+\psi), 2k\cos(\Theta+\psi)\sin\delta) \tag{A8}$$

where

$$g_{\parallel\parallel}(\tilde{\Theta}) = \frac{\varepsilon - 1}{[\cos\tilde{\Theta} + (\varepsilon - \sin^2\tilde{\Theta})^{1/2}]^2} \tag{A9}$$

$$g_{\perp\perp}(\tilde{\Theta}) = \frac{(\varepsilon-1)[\varepsilon(1+\sin^2\tilde{\Theta}) - \sin^2\tilde{\Theta}]}{[\varepsilon\cos\tilde{\Theta} + (\varepsilon - \sin^2\tilde{\Theta})^{1/2}]^2} \tag{A10}$$

E_0 is the spectrum of the short Bragg scattering waves and ε the relative dielectric constant of ocean water. For small ψ and δ the cross-section modulation (A1) is given by

$$\left(\frac{\delta\sigma}{\sigma_0}\right)_{\text{tilt}} = \frac{1}{\sigma_0}\left[\left.\frac{\partial\sigma(\Theta,\psi,\delta=0)}{\partial tg\psi}\right|_{\psi=0}\frac{\partial\xi}{\partial x} + \left.\frac{\partial\sigma(\Theta,\psi=0,\delta)}{\partial tg\delta}\right|_{\delta=0}\frac{\partial\xi}{\partial y}\right] \tag{A11}$$

Inserting the Fourier representations (1) and (2) into (A11) yields the equations (6) and (7), where $k_x = k_{\parallel}$ and $k_y = k_{\perp}$.

Acknowledgments. This work was supported in part by NATO under research grant SRG 10, the NOAA/NESS Seasat Project, and the Deutsche Forschungsgemeinschaft (SFB 94). We thank K. Hasselmann for many stimulating discussions, especially on the subject of focusing, and J. Schröter (MPI, Hamburg) for programing the formulas for the tilt modulation transfer function. This research was carried out while one of us (W.R.A.) was a visiting scientist at the NOAA Wave Propagation Laboratory in Boulder, Colorado, and the NOAA Sea-Air Interaction Laboratory in Miami, Florida.

REFERENCES

Alpers, W., and K. Hasselmann, The two-frequency microwave technique for measuring ocean wave spectra from an airplane or satellite, *Boundary Layer Meteorol., 13,* 215–230, 1978.

Alpers, W., and W. L. Jones, The modulation of the radar backscattering cross section by long ocean waves, in *Proceedings 12th International Symposium on Remote Sensing of Environment, Manila, Philippines,* pp. 1597–1607, Environmental Research Institute of Michigan, Ann Arbor, 1978.

Alpers, W. R., and C. L. Rufenach, The effect of orbital motions on synthetic aperature radar imagery of ocean waves, *IEEE Trans. Antennas Propagat., AP-27,* 685–690, 1979.

Alpers, W. R., and C. L. Rufenach, Image contrast enhancement by applying focus adjustment in synthetic aperture radar imagery of moving ocean waves, in SEASAT-SAR Processor, *ESA SP 154,* pp. 25–30, ESA Sci. and Tech. Publ. Br., ESTEC, Noordwijk, Netherlands, 1980.

Alpers, W., J. Schröter, F. Schlude, H. -J. Müller, and K. P. Koltermann, Ocean surface current measurements by an *L* band two-frequency microwave scatterometer, *Radio. Sci., 16,* 93–100, 1981.

Belousov, P. S., E. O. Zhilko, A. A. Zagorodnikov, V. I. Kornienko, V. S. Loshchidov, and K. B. Chelsev, Results of investigation of sea wave structure using a side-scan radar, In, *Proceedings of the Final Symposium on the Results of the Joint USSR/USA Bering Sea Experiment, Leningrad 12-17 May 1974,* pp. 68–79, edited by K. Ya. Kondratyev, Yu. I. Rabinovich, and W. Nordberg, editors, Gidrometeoizdat, Leningrad, 1975.

Bendat, J. S., and A. G. Piersol, *Measurement and Analysis of Random Data,* John Wiley, New York, 1971.

Bondarenko, I. M., A. A. Zagorodnikov, V. S. Loschchilov, and K. B. Tschelyshev, On the relationship between wave parameters and the spatial spectrum of aerial and radar pictures of the sea surface, Engl. Transl., *Oceanologiya, 12,* 912–919, 1972.

Brown, W. M., Synthetic aperture radar, *IEEE Trans. Aerosp. Electr. Sys., AES-3,* 217–229, 1967.

Chang, J. H., R. N. Wagner, and H. C. Yuen, Measurement of high frequency capillary waves on steep gravity waves, *J. Fluid Mech., 86,* 401–413, 1978.

Daley, J. W., W. I. Davis, and N. R. Mills, Radar sea return in high sea states, Rep., *7142,* Naval Res. Lab., Washington, D. C., 1970.

Daley, J. C., J. T. Ransone, and J. A. Burkett, Radar sea return—JOSS-I, Rep. *7268,* Naval Res. Lab., Washington, D. C., 1971.

Elachi, C. E., and W. E. Brown, Models of radar imaging of the ocean surface waves, IEEE Trans. Antennas Propagat., AP-25, 84–95, 1977.

Fontanel, A. Experiences d'étude de l'état de la mer par radar latéral, Actes de colloques, CNEXO, Brest, France, 5, pp. 309–326, 1978.

Fontanel, A., N. Lannelongue, and D. de Staerke, Etude de l'état de la mer par utilisation des hyperfréquences. Expérience Rano 1978, *Rep. 27147,* Inst. Français du Pétrole, Rueil-Malmaison (Paris), France, 1979.

Harger, R. O., *Synthetic Aperture Radar Systems,* Academic, New York, 1970.

Hasselmann, K., A simple algorithm for the direct extraction of the two-dimensional surface image spectrum from the return signal of a synthetic aperture radar, *Int. J. Rem. Sensing, 1,* 219–240, 1980.

Jain, A., Focusing effects in synthetic aperture radar imaging of ocean waves, *Appl. Phys., 15,* 323–333, 1978.

Jones, W. L., D. H. Boggs, P. Black, E. M. Bracalente, R. A. Brown, G. Dome, J. Ernst, J. L. Mitchell, S. Peterherych, W. J. Pierson, G. E. Shacher, L. C. Schroeder, D. Shelton, and F. J. Wentz, The SEASAT-A satellite scatterometer: The geophysical evaluation of remotely sensed wind vector, submitted to *J. Geophys. Res.,* 1981.

Keller, W. C., and J. W. Wright, Microwave scattering and straining of wind generated waves, *Radio Sci., 10,* 139–147, 1975.

Kraus, E. B., *Atmosphere-Ocean Interaction, Monogr. on Meteorol.,* Clarendon, Oxford, 1972.

Larson, T. R., L. I. Moskowitz, and J. W. Wright, A note on SAR imagery of the ocean, *IEEE Trans. Antennas Propagat., AP-24,* 393–394, 1976.

Lewis, B. L., and I. D. Olin, Experimental study and theoretical model of high resolution backscatter from the sea, *Radio Sci., 15,* 815–828, 1980.

Ling, S. C., A. Saad, and T. W. Kao, Mechanics of multiphase fluxes over the ocean, in *Proceedings of the NATO Conference on Turbulent Fluxes through the Sea Surfaces, Wave Dynamics, and Prediction,* pp. 185–197, edited by A. Favre and K. Hasselmann, Plenum, New York, 1978.

Long, M. W., On a two-scatter theory of sea echo, *IEEE Trans. Antennas Propagat., AP-22,* 667–672, 1974.

Long, M. W., *Radar Reflectivity of Land and Sea,* Lexington Books, Lexington, Mass., 1975.

Longuet-Higgins, G. S., and R. W. Stewart, Radiation stresses in water waves, A physical discussion with applications, *Deep Sea Res., 11,* 529–562, 1964.

Phillips, O. M., *The Dynamics of the Upper Ocean,* 2nd ed., Cambridge University Press, New York, 1977.

Phillips, O. M., and M. L. Banner, Wave breaking in the presence of wind drift and swell, *J. Fluid Mech., 66,* 625–640, 1974.

Plant, W. J., Studies of backscattered sea return with CW dual-frequency, X-band radar, *IEEE Trans. Antennas Propogat., AP-25,* 28–36, 1977.

Raney, R. K., Synthetic aperture imaging radar and moving targets, *IEEE Trans. Aerosp. Electr. Sys., AES-7,* 499–505, 1971.

Raney, R. K., SAR processing of partially coherent phenomena, *Int. J. Rem. Sens., 1,* 29–51, 1980.

Raney, R. K., and R. T. Lowry, Ocean wave imagery and wave spectra distortion by synthetic aperture radar, in *Proceedings 12th International Symposium on Remote Sensing of Environment, Manila, Phillippines,* pp. 683–702, Environmental Research Institute of Michigan, Ann Arbor, 1978.

Ross, D. B., On the use of aircraft in the observation of one- and two-dimensional ocean wave spectra, in *Ocean Wave Climate,* pp. 253–267, edited by M. D. Earle and A. Malahoff, Plenum, New York, 1978.

Ross, D. B., B. Au, W. Brown, and J. McFadden, A remote sensing study of Pacific hurricane Ava, in *Proceedings of the Ninth International Symposium on Remote Sensing of Environment,* pp. 163–180, Environmental Research Institute of Michigan, Ann Arbor, Mich., 1974.

Rufenach, C. L., and W. Alpers, Imaging ocean waves by synthetic aperture radars with long integration times, *IEEE Trans. Antennas Propagat.,* in press, 1981.

Shemdin, O. H., W. E. Brown, Jr., F. G. Staudhammer, R. Shuchman, R. Rawson, J. Zelenka, D. B. Ross, W. McLeish, and R. A. Berles, Comparison of in-situ and remotely sensed ocean waves off Marineland, Florida, *Boundary Layer Meteorol., 13,* 225–234, 1978.

Schuler, D. L., Remote sensing of directional gravity wave spectra and surface currents using a microwave dual-frequency radar, *Radio Sci., 13,* 321–331, 1978.

Shuchman, R. A., R. F. Rawson, and E. S. Kasischke, Analysis of synthetic aperture radar ocean wave data collected at Marineland and Georges Bank, final report, Environ. Res. Inst. Michigan (ERIM), Ann Arbor, 1977.

Shuchman, R. A., E. S. Kasischke and A. Klooster, Synthetic aperture radar ocean wave studies, *Final Rep. 131700-3-F,* Environ. Res. Inst. of Mich., Ann Arbor, 1978.

Swift, C. T., and L. R. Wilson, synthetic aperture radar imaging of

ocean waves, *IEEE Trans. Antennas Propagat.*, *AP-27*, 725–729, 1979.

Teleki, P. G., W. McLeish, R. A. Shuchman, D. Ross, and W. E. Brown, Jr., Ocean wave detection and direction measurements with microwave radar, in *Oceans '78—The Ocean Challenge*, pp. 639–648, Marine Technological Society, Washington, D. C., 1978.

Tomiyasu, K., Ocean wave cross radial image error in synthetic aperture radar due to radial velocity, *J. Geophys. Res.*, *80*, 45–55, 1975.

Trunk, G. V., Radar properties of non-Rayleigh sea clutter, *IEEE Trans. Aerosp. Electron.*, *AES-8*, 196–204, 1972.

Valenzuela, G. R., Scattering of electromagnetic waves from a tilted slightly rough surface, *Radio Sci.*, *3*, 1057–1066, 1968.

Valenzuela, G. R., Theories for the interaction of electromagnetic and ocean waves—A review, *Boundary Layer Meteorol.*, *13*, 61–85, 1978.

Valenzuela, G. R., An asymptotic formulation for SAR images of the dynamical ocean surface, *Radio Sci.*, *15*, 105–114, 1980.

Valenzuela, G. R., and J. W. Wright, Modulation of short gravity-capillary waves by longer-scale periodic flows, A higher-order theory, *Radio Sci.*, *14*, 1099–1110, 1979.

Valenzuela, G. R., M. B. Laing, and J. C. Daley, Ocean spectra for high frequency waves as determined from airborne radar measurements, *J. Mar. Res.*, *29*, 69–84, 1971.

Wright, J. W., A new model for sea clutter, *IEEE Trans. Antennas Propagat.*, *AP-16*, 217–223, 1968.

Wright, J. W., Detection of ocean waves by microwave radar; the short gravity-capillary waves, *Boundary Layer Meteorol.*, *13*, 101–102, 1978.

Wright, J. W., W. J. Plant, W. C. Keller, and W. L. Jones, Ocean wave-radar modulation transfer functions from the West Coast Experiment, *J. Geophys. Res.*, *85*, 4957–4966, 1980.

Yeschenko, S. D., and B. Sh. Lande, On radar mapping of sea surfaces, *Radio Eng. Electron. Phys.*, *17*, 1253–1258, 1972.

(Received June 12, 1980;
revised January 13, 1981;
accepted January 14, 1981.)